공학박사 학위논문

Active optical amplitude modulation using phase-change metasurfaces

상변이 메타표면을 이용한 능동 광학 진폭 변조

2023 년 8 월

서울대학교 대학원

전기컴퓨터공학부

김 규 호

Active optical amplitude modulation using phase-change metasurfaces

지도 교수 정 윤 찬

이 논문을 공학박사 학위논문으로 제출함
2023 년 8 월

서울대학교 대학원
전기정보공학부
김 규 호

김규호의 공학박사 학위논문을 인준함
2023 년 8 월

위 원 장 _____ (인)

부위원장 _____ (인)

위 원 _____ (인)

위 원 _____ (인)

위 원 _____ (인)

Abstract

Active optical amplitude modulation using phase-change metasurfaces

Kyuho Kim
Department of Electrical and Computer Engineering
College of Engineering
Seoul National University

The advancement of metasurface technology has enabled the miniaturization and integration of passive optical devices, such as lens, prisms, polarizers, wave plates, color filters, and mirrors. However, researchers have been focusing on developing active metasurface devices that can actively modify optical functions through external modulation signals. These active devices represent the next step in ultra-thin optical device technology. The fundamental approach to achieving active metasurfaces involves combining an optical metasurface composed of an array of nanoantenna resonators with active materials capable of changing their refractive index when subjected to external electric, thermal, or light energy. Although active metasurfaces have shown promise, there are still challenges for improvement in terms of efficiency, visible light modulation, and maximizing their versatility for various optical devices.

This dissertation presents novel research findings on three amplitude-modulated metasurface technologies utilizing vanadium dioxide thin film, a

prominent phase change material, to address the limitations of existing active metasurface devices.

First, a new design methodology and a design case for focus-switchable Fresnel zone plates (FZP) based on a phase-change aluminum-vanadium dioxide nano-absorber are proposed. By harnessing the thermo-optical effect of vanadium dioxide and the localized plasmon resonance of aluminum nanostructures, the proposed FZP design offers great design flexibility and high-contrast focus-shifting performance based on highly tunable absorption resonances.

Second, a versatile optimized active metasurface is introduced. This vanadium dioxide-based active metasurface serves as a broadband transmittance modulator that operates independently of polarization. Two distinct types of diffraction metagratings, targeting high efficiency, are designed, experimentally validated, and supported by theoretical analysis.

At last, experimental research on high-speed electro-thermal amplitude modulation in the visible light-near infrared range is conducted and the results are presented. The design incorporates gold (Au) electrical heating pad connected to vanadium dioxide to achieve electrical sensitivity and a significant modulation depth.

The proposed methods and findings in this dissertation hold potential in the development of photo-thermal and electro-thermal active optical devices for nonlinear optics, microscopy, 3D scanning, optical trapping, and holographic displays across a wide spectral range encompassing both visible and infrared regions.

Keywords: phase-change material, vanadium dioxide, metasurface, metasurface lens, nanostructure, active-metasurface
Student Number: 2013-30959

Contents

List of Table

List of Figures

Chapter 1 Introduction

1.1 Metasurface and active metasurface

In the field of nanooptics, there has been a revolutionary transformation in optical device technology over the last decade. This transformation is attributed to the emergence of metasurfaces, which are two-dimensional metamaterials capable of manipulating the wavefront of optical waves in free space. Metasurfaces enable the reduction of thickness and weight of optical devices while providing flexible control over wavefront information. They consist of densely arranged nanoantennas made of plasmonic metal or high refractive index dielectric materials, organized in a planar form with sub-wavelength periodicity. This advancement in metasurface technology opens up new possibilities for extreme miniaturization and integration of passive optical elements such as lenses, prisms, polarizers, wave plates, color filters, and mirrors [6-20]. Furthermore, the concept of active metasurfaces has gained significant attention as a next step in ultra-thin optical device technology. Active metasurfaces go beyond passive functionality by actively altering their optical properties through external modulation signals. The key approach to realizing active metasurface devices involves combining an optical metasurface, composed of an array of nanoantenna resonators, with active materials capable of changing their refractive index under external electric, thermal, or optical energy. The choice of active materials is crucial, and certain materials such as tungsten oxide [21], $Ge_2Sb_2Te_5$ (GST) [22, 23], and VO_2 [24-33] have garnered considerable interest in the optical frequency range. These materials offer

potential advancements in terms of miniaturization, modulation speed, modulation rate, and design flexibility compared to commercially available liquid crystal-based or MEMS technologies.

1.2 Characteristics of vanadium dioxide (VO_2)

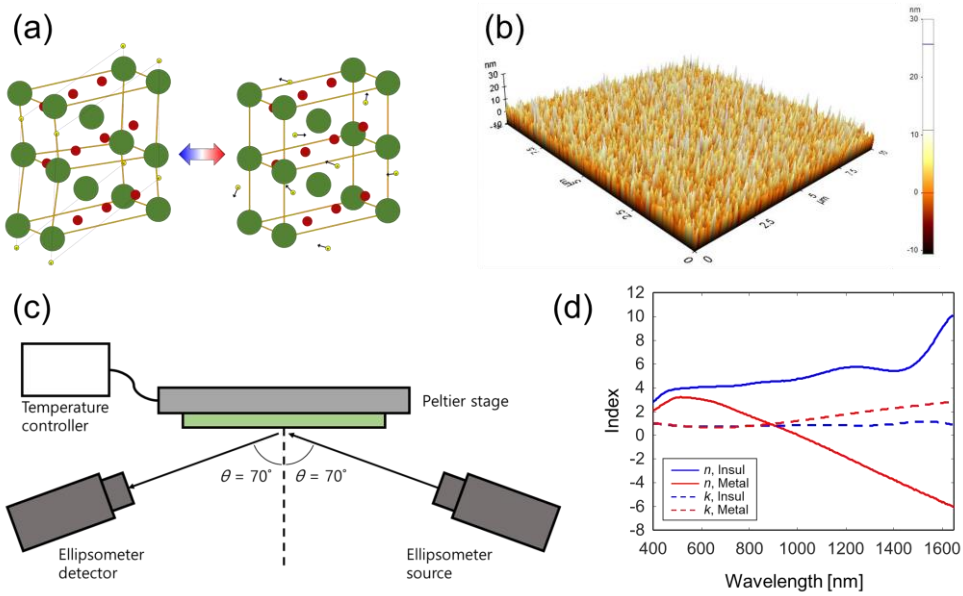

Figure 1.1 Characteristics of VO_2 (a) Schematic of the change in VO_2 crystal structure. (b) Surface of the VO_2 film (c) schematic of the ellipsometer with temperature control.

This dissertation focuses on utilizing vanadium dioxide, a representative phase change material, as the basis for an active metasurface. Vanadium dioxide offers significant advantages, particularly in the visible and near-infrared ranges, due to its high refractive index modulation factor. Compared to other candidate materials, it provides greater design flexibility in achieving desired optical modulation functions while simultaneously meeting various performance criteria such as light efficiency, modulation rate, bandwidth, and modulation speed. Vanadium dioxide undergoes a phase transition around a temperature of approximately 68 degrees Celsius, transitioning from an insulator state at room temperature to a metallic state at higher temperatures [26]. This volatile behavior enhances its appeal as a phase

change material. Figure 1.1(a) demonstrates how the arrangement of the atomic lattice undergoes a transition from a monoclinic to a tetragonal structure as the low-temperature insulating phase of VO_2 shifts to a high-temperature metallic phase. Furthermore, vanadium dioxide exhibits significant changes in refractive index and permittivity spectra over a wide frequency range. In this study, a vanadium dioxide thin film deposited on a sapphire substrate using pulsed laser deposition (PLD) was employed for research purposes [32]. Figure 1.1(b) shows the surface roughness property of a VO_2 thin film that was deposited using the PLD method obtained using atomic force microscopy (AFM). The AFM analysis reveals that the roughness of the film has a standard deviation of approximately 3.8 nm, that the thickness of the VO_2 film is around 314 nm. A notable characteristic of VO_2 is its ability to exhibit changes in optical properties, such as the dielectric function, depending on whether it is in the insulating or metallic phase. This feature adds to the interest and potential applications of VO_2. Figure 1.1(c) depicts a schematic representation of a spectroscopic ellipsometer (J.A. Woollam, V-VASE) equipped with a temperature controller. The spectroscopic ellipsometer is utilized to measure the temperature-dependent optical property of the VO2 thin film. The complex refractive index spectrum of the VO_2 film, measured in the visible and near-infrared regions, is presented in Figure 1.1(d). It is worth noting that the spectrum shows large thermo-optic tunability over the wide optical frequency range, which is highly desired for its use in design of high performance active metasurfaces.

1.3 Phase-change VO_2 metasurface

Recently, there have been numerous studies on metasurfaces utilizing thin films of vanadium dioxide [24-30]. These studies typically involve combining plasmonic or dielectric metasurfaces with vanadium dioxide films or particles. However, most of the reported research findings have encountered certain limitations. Firstly, studies focused on phase modulation suffered from reduced efficiency or were unable to achieve modulation in the visible light range. Secondly, investigations into near-infrared modulation lacked a design methodology that could simultaneously optimize performance indicators such as light efficiency, bandwidth, and modulation rate, thereby hindering practical application. Thirdly, no effective design approach has been proposed for imaging functions, such as lenses. Lastly, achieving high-speed electrical modulation in the visible range has proven to be challenging.

1.4 Purpose and organization of the dissertation

In order to overcome the limitations of the above-mentioned active phase-transition VO_2 metasurface devices, this thesis presents new research results on three amplitude modulation type metasurface technologies.

In chapter 2, novel design method and examples are presented for actively focus-switchable Fresnel Zone Plates (FZPs) using phase-change Al-VO_2 nano-absorbers. This method holds promise for potential experimental demonstrations of electro-thermal or photo-thermal switching of FZP focus, opening up possibilities for applications in active diffractive optics elements and thermally induced nonlinear optics technologies.

In chapter 3, novel multi-objective optimized metagrating devices are introduced and their performance is evaluated through numerical simulations and experimental studies. The chapter specifically focuses on two types of adjoint-optimized diffractive VO_2 metagratings, which are aimed at achieving broadband transmittance modulation for light with arbitrary polarization. The theoretical analysis conducted in the chapter provides valuable insights into the behavior of these devices, and their effectiveness is further confirmed through practical experiments. The research conducted in chapter 3 lays the foundation for the development of advanced metagrating technologies and their potential applications.

Chapter 4 examines the electrical modulation of reflected light amplitude in the visible and near-infrared bands using reflective VO_2 nanostructures. The chapter presents experimental results for both DC and AC modulation via electrical current source. The findings suggest that VO_2 is capable of achieving relatively fast

modulation. The chapter then explores the potential applications and implications of this electrical modulation property. By leveraging the unique capabilities of VO_2, there are opportunities for advancements in various fields.

Finally, the concluding remarks are provided in Chapter 5.

Chapter 2 Design of dynamic focus – switchable Fresnel zone plates based on plasmonic phase-change VO_2 metafilm absorvers

2.1 Introduction

In the field of nanophotonics, optical metasurfaces made of dielectrics and metals have risen as promising next-generation diffractive optical element technologies by virtue of the extensive capabilities of engineering an on-demand arbitrary wavefront [1, 2], absorption and scattering spectra [3], polarization selectivity and multi-functionality [4], and even the dynamic tunability of designated optical functions [5]. In particular, beam steering and imaging functions with optical metasurfaces, metagrating deflectors [6-11] and metalenses [12-20] with sub-micron thicknesses have been the most popular and significant applications in free space. Since the seminal papers on phase-gradient metasurfaces by the Capasso group in Harvard University [1] and Brongersma group in Stanford University [2], countless studies have been conducted to demonstrate advanced metagratings and metalenses with improved performance [6-20].

On the other hand, relatively less progress has been achieved with dynamically tunable optical metasurfaces where designated wavefront shaping functions can be switched or gradually tuned by active optical materials and corresponding external stimuli [5]. The main obstacle has been the lack of excellent optical material with large tunability, high refractive index (RI), and low intrinsic absorption in the visible and near-infrared regimes. Vanadium dioxide (VO_2), a representative phase-change material, has been

widely studied for the relatively good thermo-optic tunability of the optical dielectric function despite considerable absorption loss [11, 24-33]. Since VO_2 exhibits large thermo-optic tunability over the visible to infrared range, various VO_2 based metasurfaces have been developed and tuned in thermo-optic and electro-thermo-optic manners. However, due to the intrinsically large absorption of VO_2, dynamic phase modulation in the phase-change metasurface has rarely been achieved with high optical efficiency [28]. On the other hand, it has been proved that amplitude modulators based on the phase change of VO_2 metasurfaces would be more useful and realizable for the multi-objective design of optical functions [11, 30-32].

In this chapter, I propose a novel design of thermo-optically focus-switchable Fresnel zone plates (FZPs) based on phase-change Gires-Tournois type metafilm (MF) absorbers [32-38]. To simultaneously increase numerical aperture (NA), focus switching contrast (SC), and focusing efficiency, we adopt four different types of reflection-type Al-VO_2 MF structures as the building blocks of the reflection-type FZPs. These building blocks based on a Gires-Tournois interferometer with deep subwavelength thickness [32-38] are judiciously engineered to provide four distinct reflectance modulation functions.

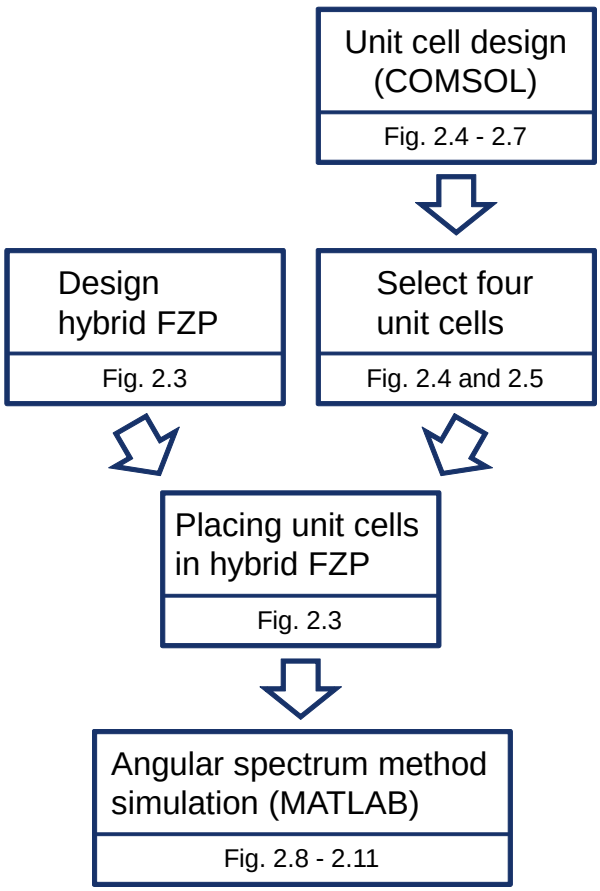

Figure 2.1 Process of design and analysis of dynamic focus switchable Fresnel zone plates

The chapter is organized as follows. First, the concepts and goals of the actively tunable FZPs are described in detail. Then, design principles based on electromagnetic simulations and scalar wave diffraction theory are suggested. Lastly, the focus-switching performances of the designed FZPs are analyzed. The electromagnetic full field and scalar wave diffraction simulations are performed by the finite element method (COMSOL Multiphysics RF solver; COMSOL, MA, USA) and customized angular spectrum method code written in MATLAB, respectively. This process is shown in Figure 2.1.

2.2 Method and Results Concept and goal

2.2.1 Concept and goal

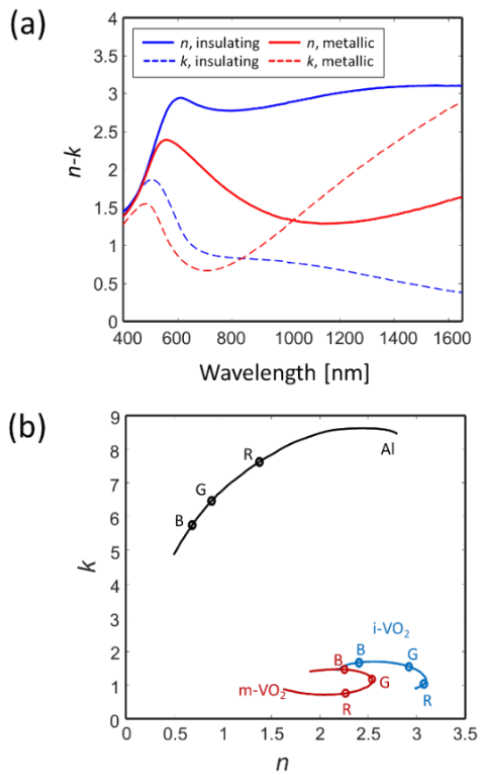

Figure 2.2 Optical property of VO_2. (a) Spectra of refractive indices and extinction coefficients of insulating and metallic VO_2 thin films. (b) Complex refractive index map of Al, and insulating and metallic VO2 phases. B, G, and R represent the blue (473 nm), green (532 nm), and red (660 nm) wavelengths, respectively.

Figure 2.2(a) describes the results of our previous measurement of the complex RI spectra of 50-nm-thick VO_2 thin film grown by the pulsed-laser deposition method in the optical regime [32]. Owing to the large thermo-optic SC of the complex RI of our data, it is possible to design visible-range focus-switching FZPs with high NA and SC. The idea to design highly tunable MF unit cells is to use reflection-type tunable plasmonic absorption resonance similar to our previous work [32].

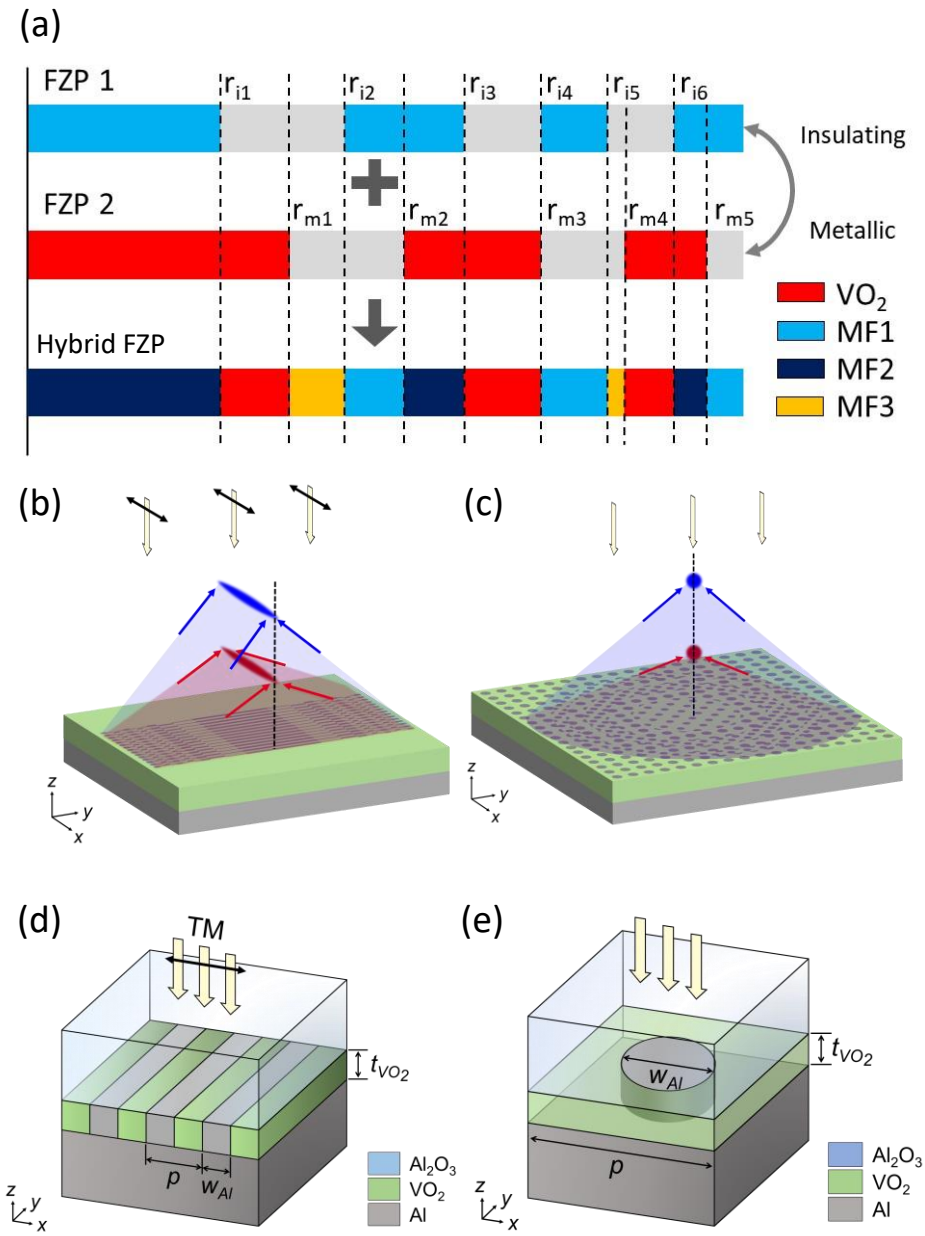

Figure 2.3 Concepts of the focus-switchable FZPs. (a) Diagram of the design of amplitude profiles of active focus-switchable Fresnel zone plates (FZPs). Schemes describing the thermally focus-switchable (b) cylindrical and (c) spherical lenses. The red and blue foci in (c) and (d) imply the foci in the metallic (heated) and insulating (room temperature) phases, respectively. The type metafilm (MF) unit cell structures for (d) cylindrical and (e) spherical lenses. The unit cell configurations of (d) and (e) are based on 50-nm-thick VO_2 film grown on an Al_2O_3 substrate and covered by a thick Al reflector

As the first step ahead of the simulations, Al is chosen as the plasmonic material that will be embedded as nanostructures inside the 50-nm-thick VO_2 thin film and used as a back reflector.

The RI data of Al [39] and Al_2O_3 [40] are cited from the literature. According to the complex RI map described in Figure 2.2(b), it is clearly seen that the complex RI coordinates of Al are very far from VO_2 in both phases in the visible range. Therefore, when Al-VO_2 MF is engineered with composites of the two materials, it would be possible to design largely different thermally tunable effective RI and reflection amplitudes from MFs by tuning the filling factor and shape of Al nanostructures [32, 41-43].

To build a focus-switchable FZP, a switchable hybrid profile of reflection amplitude is required. The FZP1 and FZP2 depicted in Figure 2.3(a) correspond to amplitude profiles in the insulating and metallic phases for different focal lengths, respectively. In Figure 2.3(a), the gray regions in FZP1 and FZP2 denote temperature-independent highly reflective regions, while the sky blue and red regions in FZP1 and FZP2 refer to nearly reflectionless regions. FZP1 and FZP2 with different focal lengths have different sets of radii of Fresnel zones according to the following Eq. (1).

$$r_n = \sqrt{n\lambda f + \frac{1}{4}n^2\lambda^2} \ . \qquad (2.1)$$

Equation (1) dictates the design principle of the nth order Fresnel zone radius (rn) depending on the wavelength. Here, n, λ, and f refer to the order of Fresnel zone, wavelength in a medium (Al_2O_3 substrate), and focal length, respectively.

Since the two FZP profiles are to be merged into a single FZP [the third profile in Figure 2.3(a)], it is necessary to deploy four different unit cell building blocks that provide different thermo-optic tunability of reflectance. The building blocks would play four different roles as tunable or not tunable reflectors depending on the phase change of VO_2. The required unit cells are temperature-dependent switchable near-unity absorbers (bare VO_2 with Al mirror, MF1), temperature-independent near-unity absorbers (MF2 for passive near-zero reflection), and temperature-independent weak absorbers (MF3 for passive high reflection). In particular, the most important unit cells are bare VO_2 with Al reflector and MF1. The former acts as a near-unity absorber only in the insulating phase, while the latter acts as a near-unity absorber only in the metallic phase of VO_2. This implies that the region of bare VO_2 with an Al mirror reflects considerable light only in the metallic phase, while MF1 acts as a reflector only in the insulating phase, in the opposite manner.

With the abovementioned hybridization of the two FZPs with different focal lengths, high-NA focus switching in both 2D [Figure 2.3(b)] and 3D [Figure 2.3(c)] FZPs can be designed. For a demonstration of the unit cells of a 2D cylindrical lens and 3D spherical FZP lens, schemes of VO2 MFs containing embedded Al nanobeams [Figure 2.3(d)] and nanodisks [Figure 2.3(e)] are used, respectively.

2.2.2 Design principles

The detailed electromagnetic design procedure is as follows. First, the target wavelength is set to be 660 nm (red) considering the large thermo-optic tunability at this wavelength. Second, for several unit cell periods, the filling factor of Al embeddings (f_{Al}) in 50-nm-thick VO_2 film capped by an Al reflector and a sapphire substrate is engineered to find the four unit cells.

Through the parameter sweeps of f_{Al} by varying the Al nanobeam width and nanodisk radius (for several values of periods), the optimal geometric parameters for MF1, MF2, and MF3 are determined for 2D and 3D cases as shown in Figure 2.4 and 2.5, respectively. Figures 2.4(a)-2.4(c) represent the modulation depth spectra according to the f_{Al} of the 2D unit cell, while Figures 2.5(a)-2.5(c) represent those of 3D cases obtained from electromagnetic full-field simulations. Here, modulation depth (η) is defined as the normalized value between 0 and 1, $\eta = |R_i - R_m|/\max(R_i, R_m)$. R_i and R_m refer to reflectance in the insulating and metallic phases, respectively.

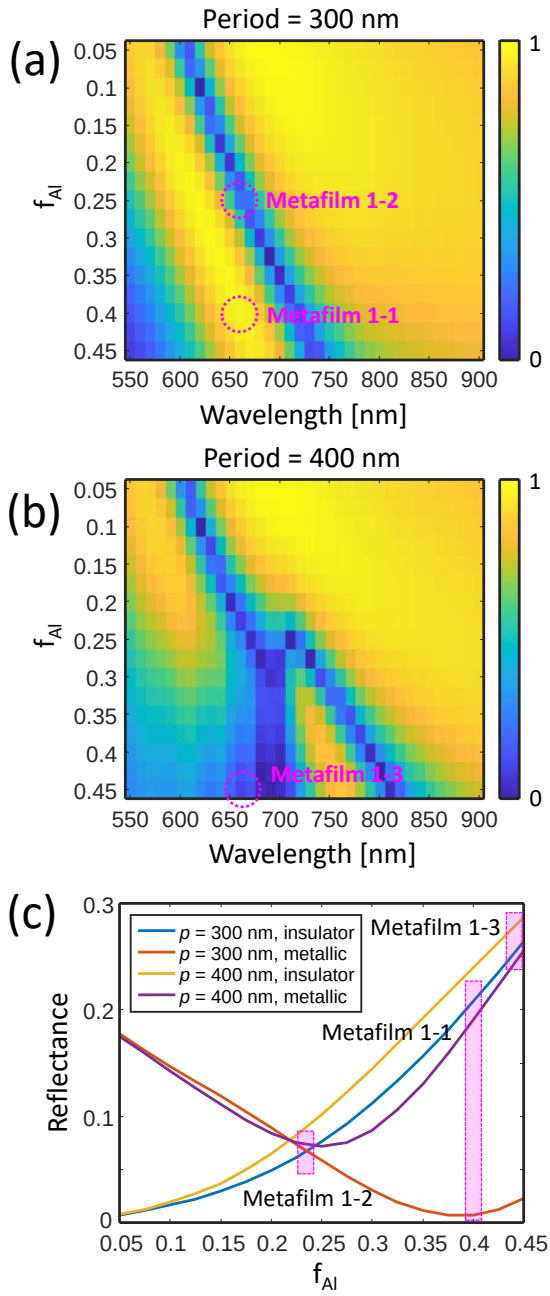

Figure 2.4 Simulated modulation depth spectra according to the filling factor of aluminum nanobeams when the period is (a) 300 nm and (b) 400 nm. (c) Effect of Al nanobeam filling factor on reflectance at the wavelength of 660 nm.

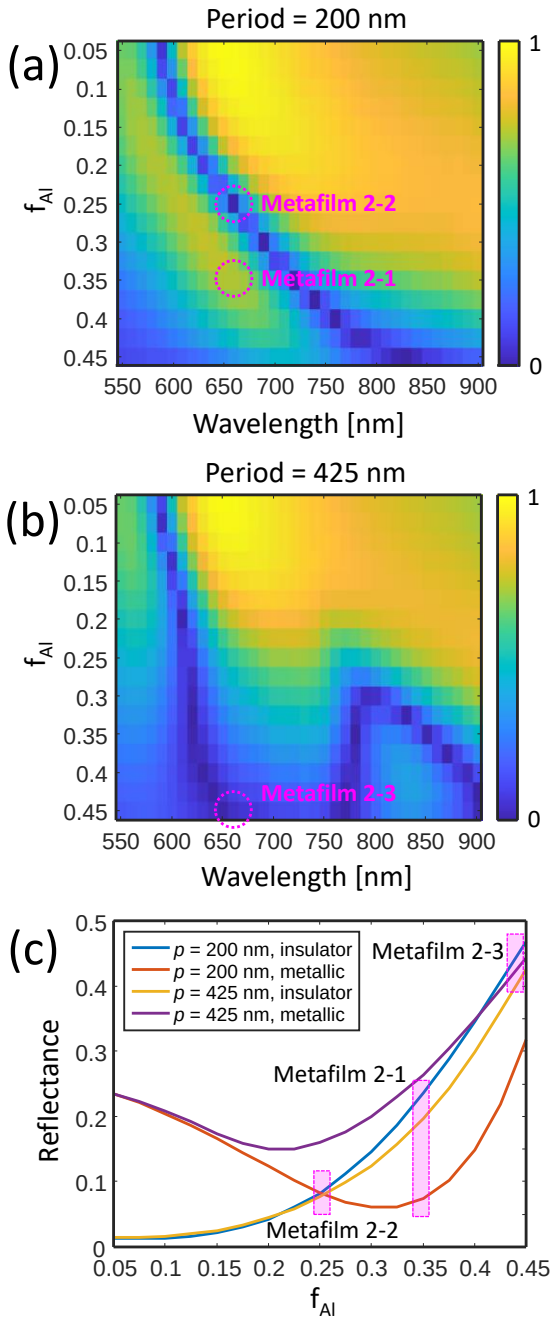

Figure 2.5 Simulated modulation depth spectra according to the filling factor of aluminum nanodisks when the period is (a) 200 nm and (b) 425 nm. (c) Effect of Al nanodisk filling factor on reflectance at the wavelength of 660 nm.

At the target wavelength, design parameters (unit cell period and f_{Al}) are chosen by considering modulation depth and reflectance. When MF1 is engineered, geometric parameters are chosen to make the modulation depth reach a near-unity value. On the contrary, MF2 (temperature-independent perfect absorber) and MF3 (temperature-independent strong reflector) are designed to exhibit a near-zero modulation depth. The pink marks in the modulation depth spectra in Figures 2.4(a), 2.4(b), 2.5(a), and 2.5(b) refer to the MF1, MF2, and MF3 parameter conditions of 2D and 3D FZPs, respectively. The effects of chosen sets of the unit cells are seen in the plots in Figure 2.4(c) and 2.5(c) and the figures show that our design goal is achieved. In particular, when f_{Al} reaches 0.4 and 0.35 for the 2D nanobeam and 3D nanodisk schemes, respectively, the MF1 unit cells for 2D cylindrical and 3D spherical FZPs are well designed as near-perfect absorbers only in the metallic phase of VO_2. On the other hand, zero-valued f_{Al} (bare VO_2 without Al embedding) acts oppositely, as a near-perfect absorber only in the insulating phase of VO_2. The detailed design parameters of the unit cells are summarized in Table 2.1.

The main reasons for switchable and non-switchable reflection amplitudes from FZP unit cells originate from nanoscale absorption resonances [32]. Figure 2.5(a) shows that reflectance from an ultrathin Gires-Tournois VO_2 film absorber can be largely tuned by virtue of near-unity absorption in the insulating phase and the thermal RI change of VO_2 film [32, 37].

TABLE 2.1 Geometric parameters of unit cells

FZP unit cells	f_{Al}	p (nm)	w_{Al} (nm)
Bare VO_2 with reflector	0	0	0
2D MF1 (MF1-1)	0.4	300	120
2D MF2 (MF1-2)	0.24	300	72
2D MF3 (MF1-3)	0.45	400	180
3D MF1 (MF2-1)	0.35	200	133
3D MF2 (MF2-2)	0.25	200	112
3D MF3 (MF2-3)	0.45	425	322

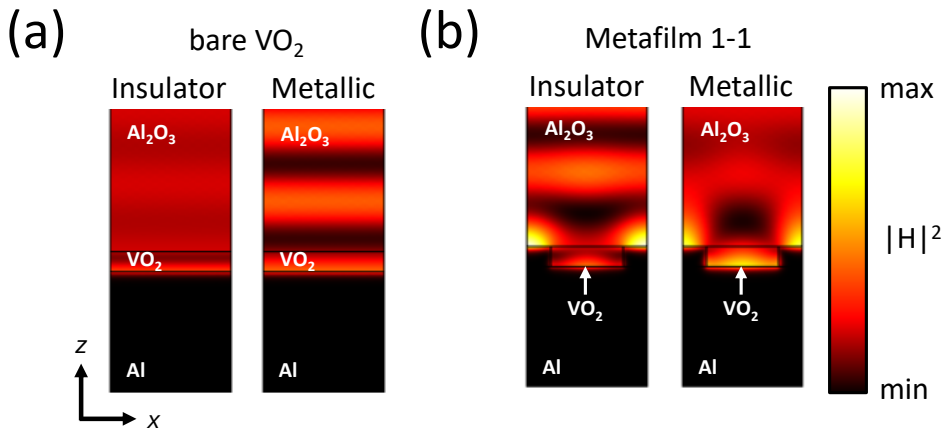

Figure 2.6 Magnetic field intensity profiles of Fresnel zone plate (FZP) unit cells, (a) bare VO_2 on Al and (b) MF 1-1 in both phases of VO_2. (a) and (b) depict field profiles on the *xz*-plane.

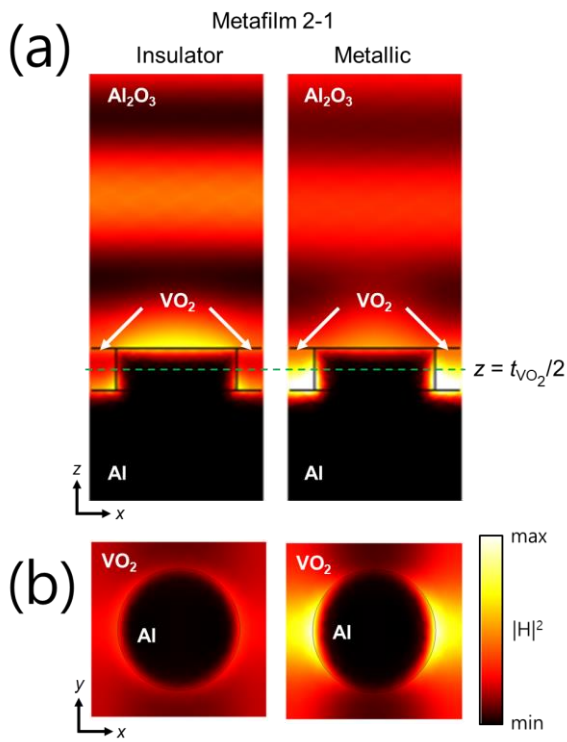

Figure 2.7 Magnetic field intensity profiles of Fresnel zone plate (FZP) unit cells, (a) and (b) MF 2-1 in both phases of VO_2. (a) depicts field profiles on the *xz*-plane while (b) shows *xy*-plane profiles on a cross section in the middle of the VO_2 film thickness.

Embedded Al nanostructures in MFs are designed to move positions of absorption resonances in both phases of VO_2 in desired ways due to the tuning of localized surface plasmon resonances. In Figures 2.3(c) and 2.4(c), the effects of Al filling factor for reflectance shift are suggested for the target wavelength. The cooling and heating of the device shift the resonance position toward shorter and longer wavelengths according to the red and blue shift of the VO_2 RI, respectively. The field profiles of Figures 2.5(b) and 2.6(a) graphically show that absorption in VO_2 of MF1-1 and MF2-1 are enhanced by the Al nanostructures in the metallic phase so that they act as near-unity absorbers only in the metallic phase.

2.2.3 Results: Design of cylindrical and spherical FZPs

In this section, the switchable focusing performance of designed cylindrical (2D) and spherical (3D) FZPs is investigated with scalar wave optics simulation. As mentioned in the first section, the simulation results presented in Figure 2.7 and 2.8 are produced by simulation codes based on the angular spectrum method of scalar wave optics using fast Fourier transform in MATLAB. Since our devices exhibit high NA focusing properties, Fresnel or Fraunhofer diffraction for paraxial approximation is not adequate for this case.

As illustrated in Figure 2.7 and Figure 2.8, high-contrast focus switching between two microscale FZPs (diameter: 20 μm) with largely different focal lengths (3 and 6 μm) is successfully achieved.

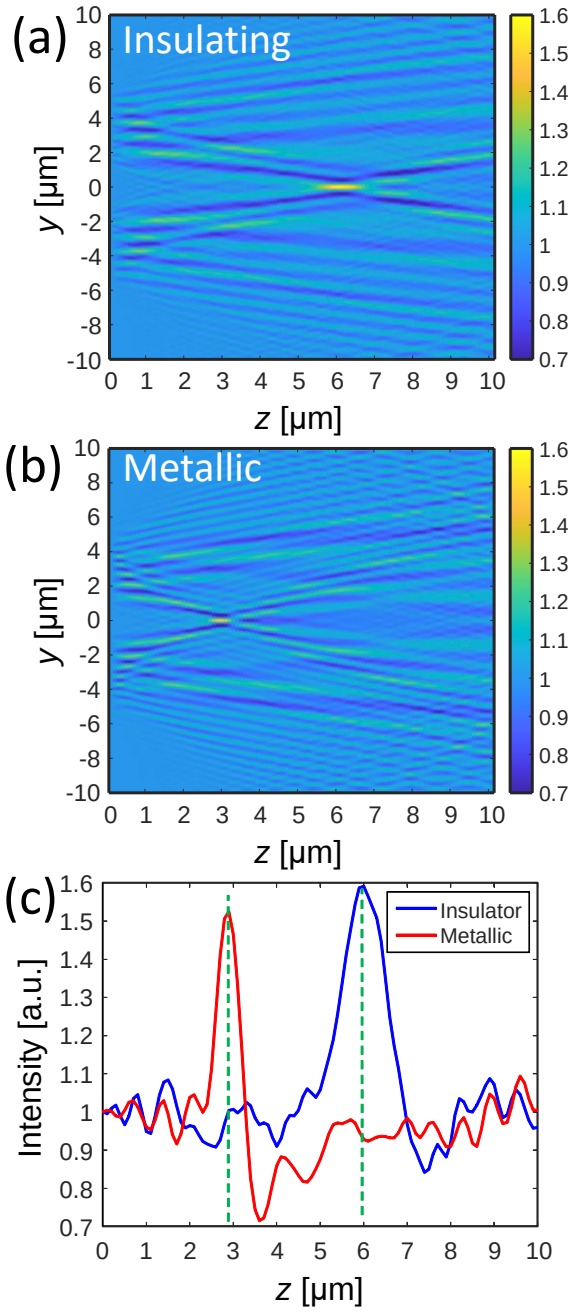

Figure 2.8 Simulation results of temperature-dependent focusing and switching of a 2D cylindrical lens. Diffraction intensity maps in the (a) insulating (room temp.) and (b) metallic (hot) phases of VO_2 on the *yz* plane. (c) Focus-switching contrast along the optic axis. The blue and red lines denote the insulating and metallic phases of VO_2, respectively.

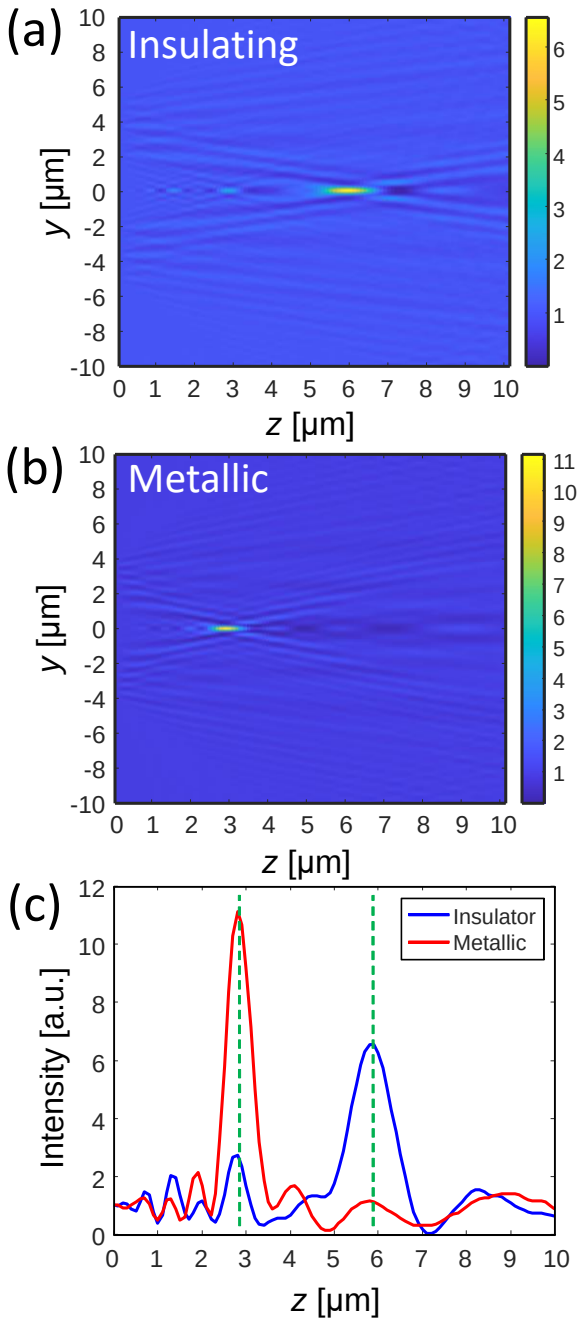

Figure 2.9 Simulation results of temperature-dependent focusing and switching of a 3D spherical lens. Diffraction intensity maps in the (a) insulating (room temp.) and (b) metallic (hot) phases of VO_2 on the *yz* plane. (c) Focus-switching contrast along the optic axis. The blue and red lines denote the insulating and metallic phases of VO_2, respectively.

The quantitative performances of focusing and switching are summarized in Tables 2 and 3. The SC is defined as SC = $(I_{max}-I_{min})/(I_{max}+I_{min})$ in percentage. I_{max} and I_{min} are the maximum and minimum intensity along the optic axis, which can be found in Figures 2.7(c) and 2.8(c). When it comes to full width at half maximum (FWHM) at the cross-section of the focal point, the sizes of the main lobes of the 2D (Figure 2.9) and 3D foci (Figure 2.10) resemble diffraction-limited Airy disks in both phases of VO_2. However, in Figures 2.9 and 2.10, it is seen that the 3D spherical lens has better focusing quality compared to that of the 2D cylindrical one. The difference in focusing quality seems to come from the difference in the switching quality of the sets of the 2D and 3D unit cells suggested in Figures 2.3 and 2.4, respectively.

TABLE 2.2 Focusing performance: 2D cylindrical Fresnel zone plate (FZP)

Lenses	Focal length (μm)	NA	Focusing efficiency (%)	FWHM (nm)	Switching contrast (%)
FZP1 (Insulating)	5.90	1.52	2.67	363.85	23
FZP2 (Metallic)	2.90	1.70	1.84	210.70	25

TABLE 2.3 Focusing performance: 3D spherical Fresnel zone plate (FZP)

Lenses	Focal length (μm)	NA	Focusing efficiency (%)	FWHM (nm)	Switching contrast (%)
FZP1 (Insulating)	5.90	1.52	9.31	341	40
FZP2 (Metallic)	2.80	1.70	13.47	250	83

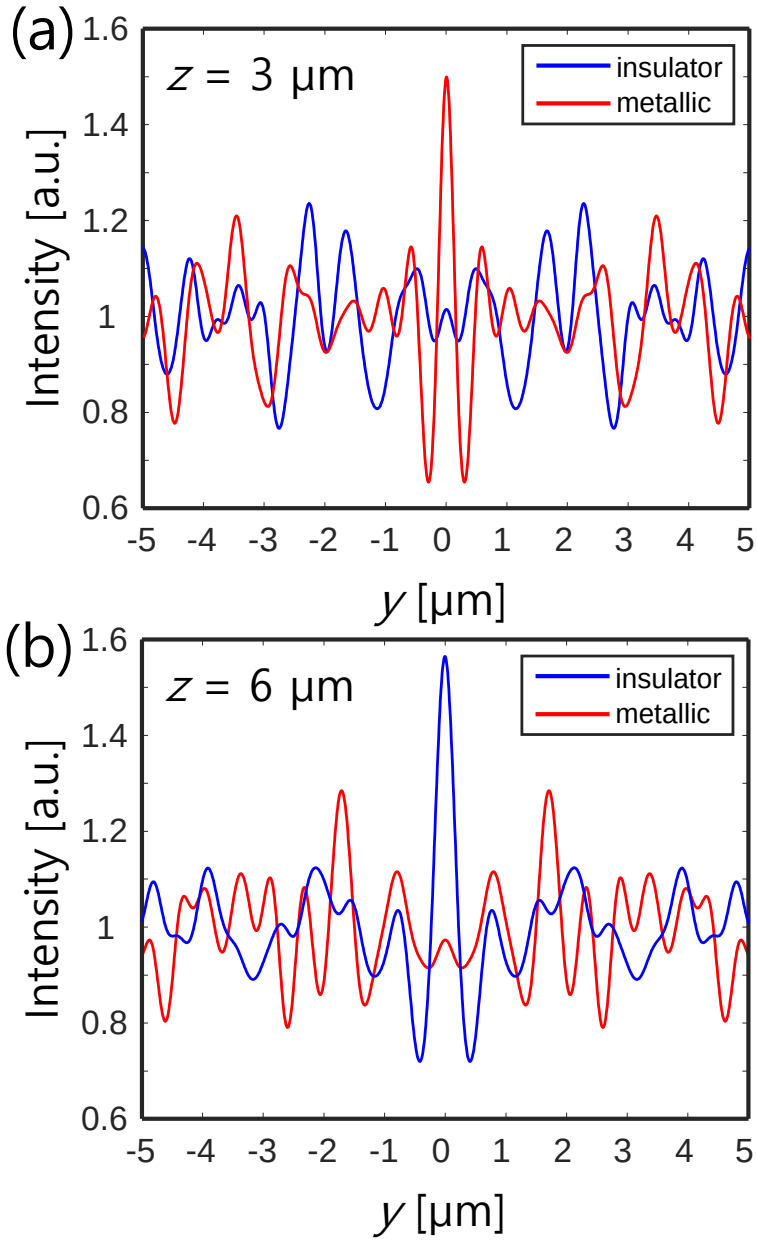

Figure 2.10 Cross-sectional focusing properties (magnetic field intensity) of a switchable 2D cylindrical Fresnel zone plate (FZP) at the designated focal points at (a) $z = 3$ μm and (b) $z = 6$ μm, respectively.

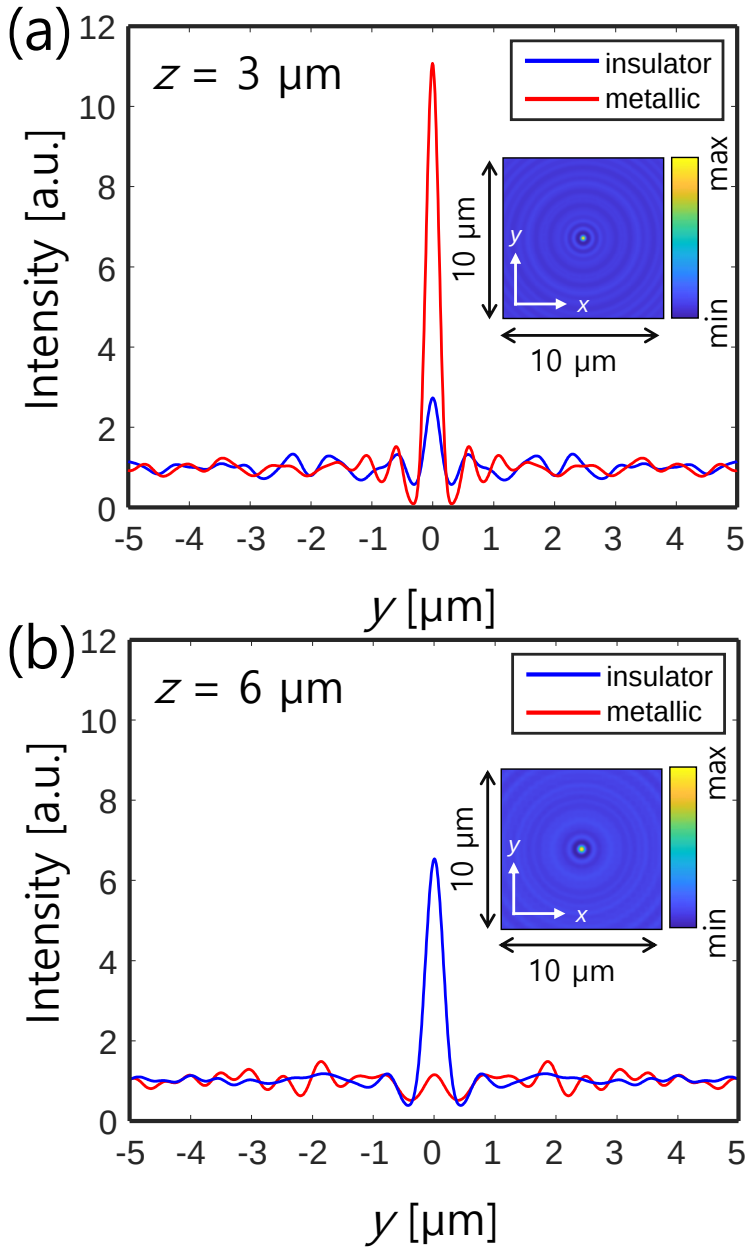

Figure 2.11 Cross-sectional focusing properties (electric field intensity) of the switchable 3D spherical Fresnel zone plate (FZP) at the designated focal points at (a) $z = 3$ μm and (b) $z = 6$ μm. The inset figures are 2D focusing profiles in the (a) metallic and (b) insulator phases of VO_2.

The most noteworthy point to discuss implied from Tables 2.2 and 2.3 is focusing efficiency. The theoretical maximum efficiency limit of FZP1 and FZP2 are 6.31 and 4.39 % at 2D and 72.79 and 27.35 % at 3D configurations, respectively. Since our device is based on the amplitude modulation method of FZP and largely tunable absorption resonances for the unit cell designs, a drop in focusing efficiency is inevitable.

Based on the proposed principles, focusing efficiency and quality could be further improved if an additional lossless dielectric thin film resonator is vertically stacked on the Al-VO_2 MFs to increase the reflectance of the unit cells [32]. By inserting an additional thin film resonator, it could be possible to enhance the reflectance of MFs for higher focusing efficiency and quality with a negligible decrease in the modulation depth of the unit cells. The 2D unit cell configuration depicted in Figures 2.12(a) and 2.12(b) illustrates an example of the abovementioned idea. Insertion of a lossless Si_3N_4 film [44] can provide an additional design degree of freedom so that the reflectance of the bare reflector (in the metallic phase), MF1-1 (in the insulating phase), and MF1-3 (in both phases of VO_2) could be further increased. Some improvement of reflectance of the 2D FZP unit cells is found in our parameter sweep simulations [Figure. 2.12(c)] compared to the original design without the Si_3N_4 film. In addition, we expect that multi-variable geometry optimization based on numerical algorithms [45], considering f_{Al}, the thickness values of VO_2, Al_2O_3 spacer, and Si_3N_4, and the unit cell period, could push the efficiency and quality of focusing to the ideal limit to some degree.

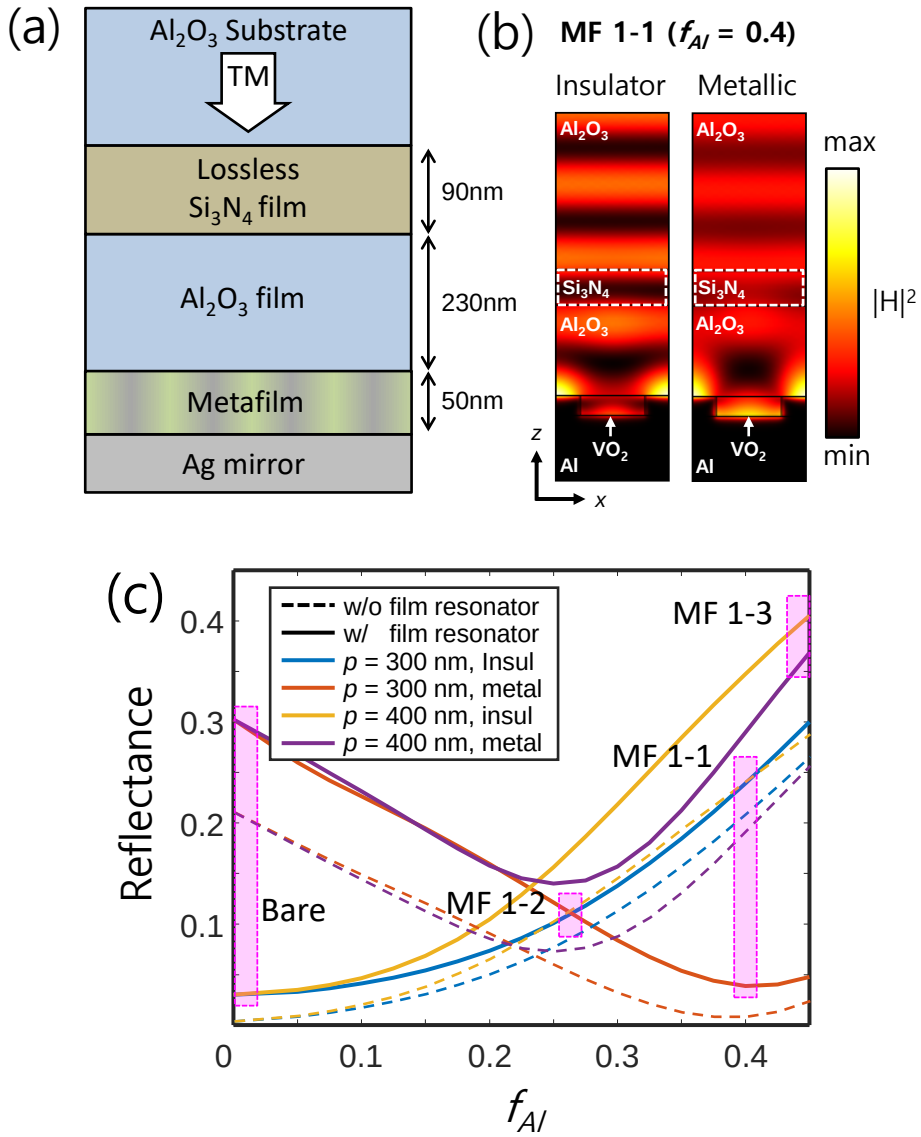

Figure 2.12 (a) Schematic diagram of a switchable 2D MF unit cell with a 90-nm-thick film Si_3N_4 resonator with a 230-nm-thick Al_2O_3 spacer. (b) Magnetic field intensity profiles of the new MF 1-1 unit cell (f_{Al} = 0.4) in the insulator (left) and metallic (right) phases. (c) Effect of the Al nanobeam filling factor on reflectance at the wavelength of 660 nm. The bold and dotted lines in (c) refer to reflectance with and without the Si_3N_4 film, respectively. The four colored legends in (c) account for the different unit cell periods and phases of VO_2.

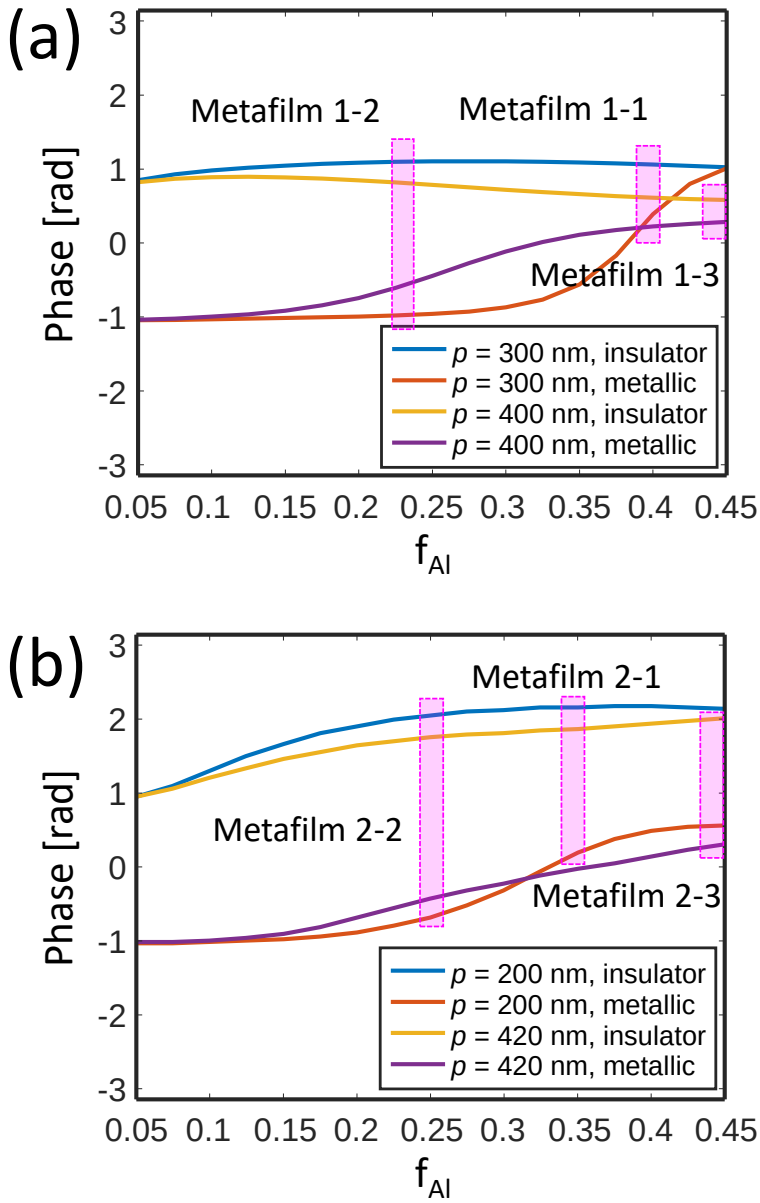

Figure 2.13 Effect of of Al (a) nanobeam and (b) nanodisk filling factor on phase of reflect light at wavelength of 660 nm.

Figure 2.13 is shown that the phase of reflected light at a wavelength of 660 nm is influenced by the filling factors of Al nanobeams (Figure 2.13(a)) and nanodisks (Figure 2.13(b)). The pink markers represent the selected filling factors MF1, MF2, and MF3 from Figures 2.4 and 2.5. Additionally, it can be observed that one of the reasons for the superior focusing quality of the 3D spherical lens compared to the 2D cylindrical lens is also shown here. When VO2 is in either the insulating or metallic phase with the same phase, the phase difference of the reflected light from the unit cells is smaller for the 3D spherical lens, as seen in Figure 2.3. Therefore, the quality of the 3D spherical lens with less phase difference is superior.

The performance of the proposed lens was compared to that of an ideal FZP lens. Figure 2.14 demonstrates the focal switching of the ideal 2D cylindrical lens with a reflection coefficient composed of only 0s and 1s. The performance of the proposed 2D cylindrical lens (Table 2.2) is lower overall compared to the ideal lens (Table 2.4). However, the proposed design maintains the high NA and focal switching performance targeted in this chapter. Furthermore, when comparing the diffraction intensity maps of the proposed design and the ideal lens, it can be observed that in both the insulating (Figure 2.8(a) and Figure 2.14(a)) and the metallic phase of VO_2 (Figure 2.8(b) and Figure 2.14(b)), the areas where diffracted waves exhibit constructive interference show a striking similarity in intensity enhancement. This similarity is particularly evident in the magnified diffraction intensity maps at the outermost boundaries (Figure 2.15). Therefore, the simulation results obtained using the angular spectrum method can be trusted.

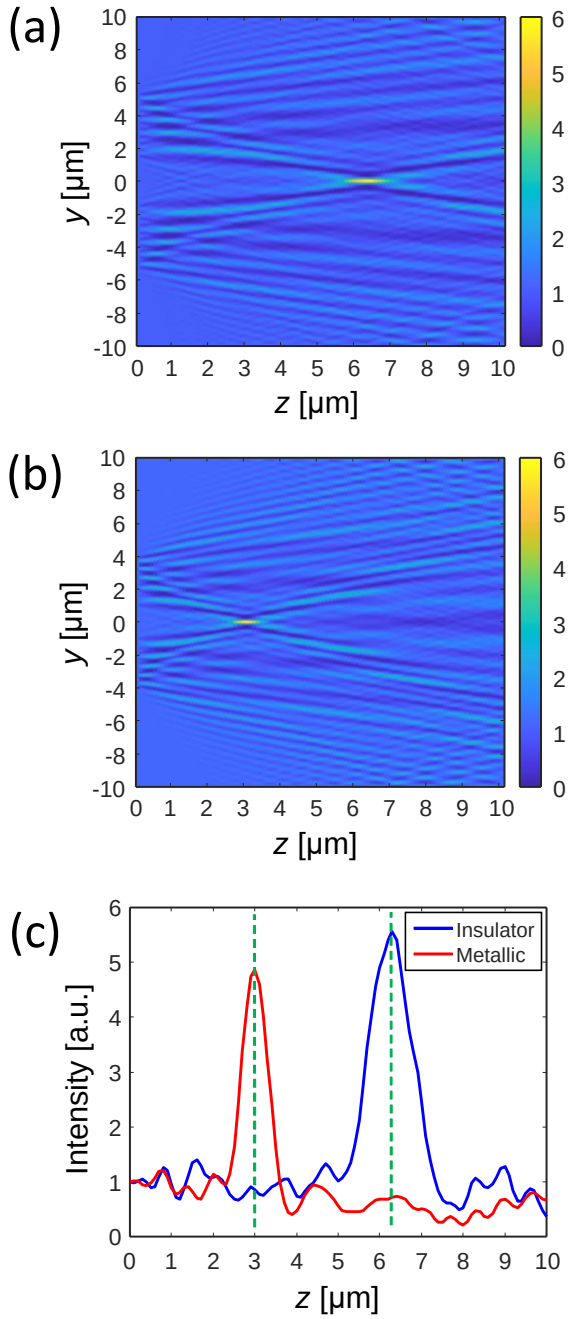

Figure 2.14 Simulation results of temperature-dependent focusing and switching of an ideal 2D cylindrical lens. Diffraction intensity maps in the (a) insulating (room temp.) and (b) metallic (hot) phases of VO_2 on the *yz* plane. (c) Focus-switching contrast along the optic axis. The blue and red lines denote the insulating and metallic phases of VO_2, respectively.

TABLE 2.4 Focusing performance: Ideal 2D cylindrical Fresnel zone plate (FZP)

Lenses	Focal length (μm)	NA	Focusing efficiency (%)	FWHM (nm)	Switching contrast (%)
FZP1 (Insulating)	6.30	1.49	2.65	269.69	73.05
FZP2 (Metallic)	3.00	1.69	4.61	223.11	74.58

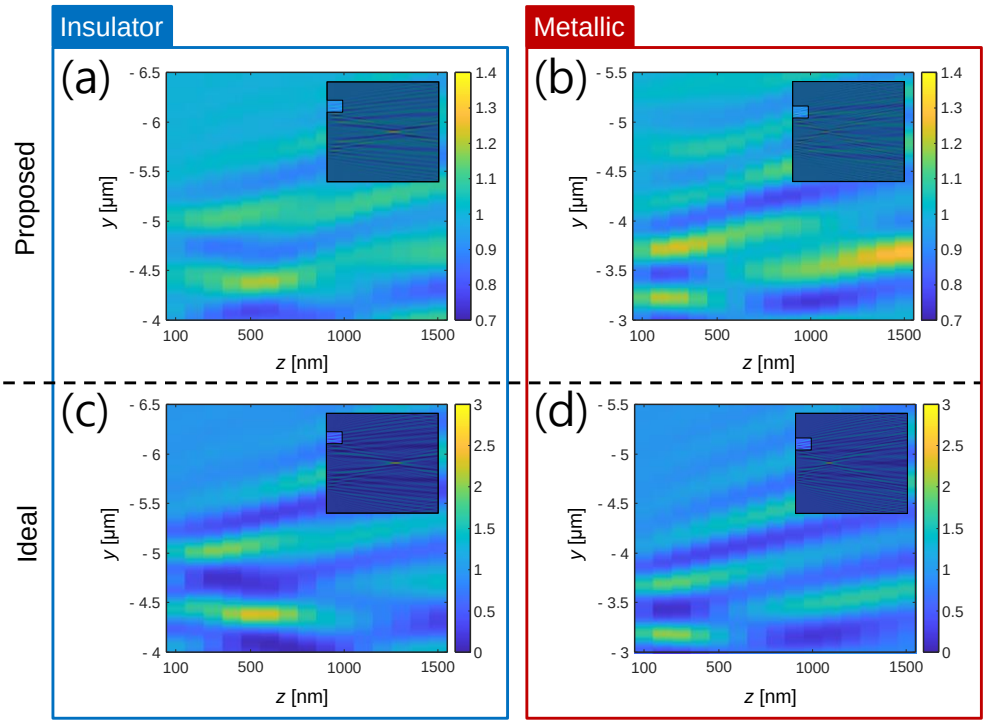

Figure 2.15 Simulation results of temperature-dependent focusing and switching of a (a), (b) proposed and (c), (d) ideal 2D cylindrical lens. Magnified diffraction intensity maps in the (a), (c) insulating (room temp.) and (b), (d) metallic (hot) phases of VO2 on the *yz* plane. The inset images highlight the magnified portions within the overall simulation range for each case.

When fabricating the hybrid FZP, an additional factor to consider is the placement of unit cells. As shown in Figure 2.16, if a unit cell is not adequately included within the block of the hybrid FZP, that particular area will not function according to the desired unit cell's performance. Figures 2.17 show the simulation

results after removing cases where the unit cells of the MF2-3 were not sufficiently included in the FZP block. Similar to the original design, it can be observed that the focus is achieved around 3 μm and 6 μm. The performance of this lens can be seen in Table 2.5. When compared to the performance of the original structure in Table 2.3, there is an overall degradation in performance, but the focusing efficiency and switching contrast improve in the metallic phase. This is because the removed MF2-3 area has a greater influence in achieving focus in the insulating phase.

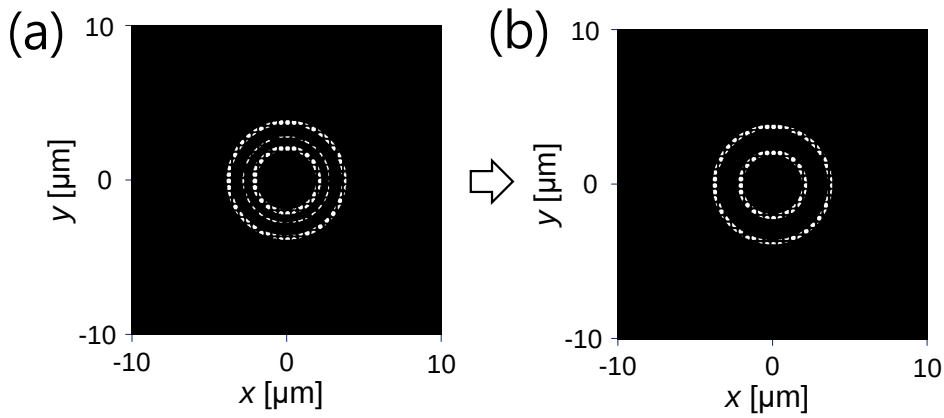

Figure 2.16 In a spherical lens, MF2-3 is placed as follows: (a) the proposed lens and (b) the lens that cases where unit cells of MF2-3 are not sufficiently included in the FZP block have been removed

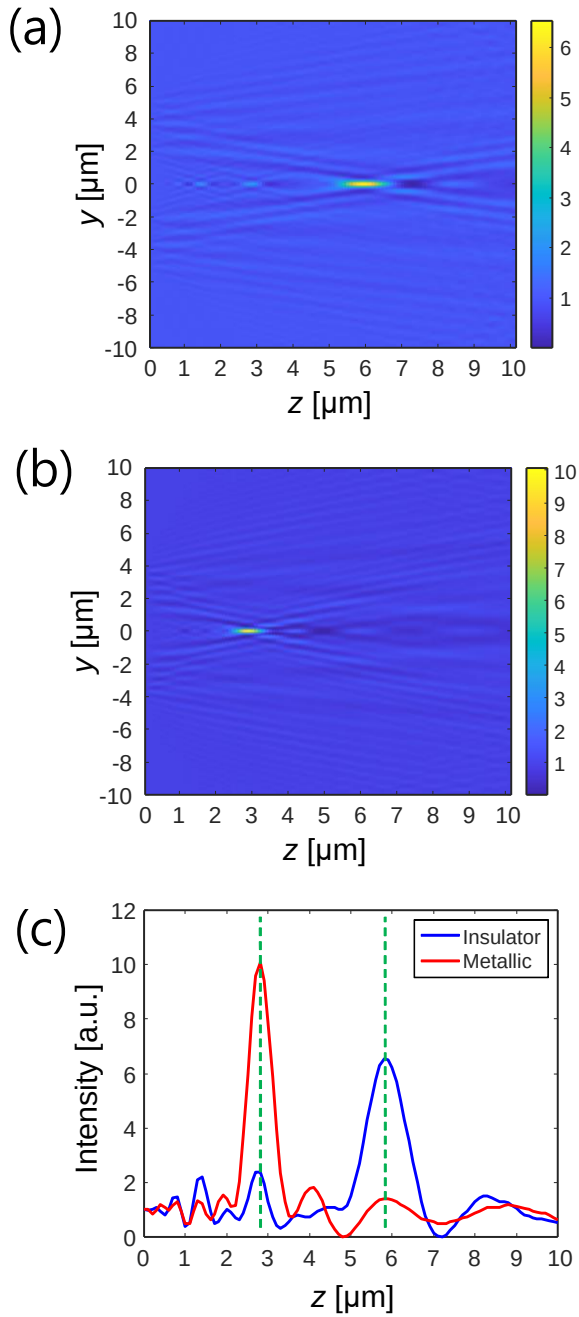

Figure 2.17 Simulation results of temperature-dependent focusing and switching of an 3D cylindrical lens with removed insufficient block. Diffraction intensity maps in the (a) insulating (room temp.) and (b) metallic (hot) phases of VO_2 on the *yz* plane. (c) Focus-switching contrast along the optic axis. The blue and red lines denote the insulating and metallic phases of VO_2, respectively.

TABLE 2.5 Focusing performance: 3D cylindrical Fresnel zone plate (FZP) with removed insufficient block.

Lenses	Focal length (μm)	NA	Focusing efficiency (%)	FWHM (nm)	Switching contrast (%)
FZP1 (Insulating)	5.80	1.53	9.20	335.2	46.59
FZP2 (Metallic)	2.80	1.69	10.15	245.16	75.46

A comparative analysis of the lens performance between the proposed device and existing studies was conducted in Table 2.5. Five different studies implementing switchable focus were examined in terms of design principles, target wavelength, reconfiguration material, focal length, NA, focusing efficiency, FWHM, and switching contrast. It is noteworthy that the structure proposed in this chapter operates in the visible light range while achieving the shortest focal length and the highest NA value.

TABLE 2.6 Comparison of focus-switching mechanism and performance with the recent representative studies

Ref.	**Design principle**	**Reconfigurable material and**	**Focal length (μm)**	**Focusing efficiency (%)**	**FWHM (μm)**
		operation wavelength (nm)	**NA**		
M. Wang et al., [46]	Mie-type resonance	Sb_2Se_3	50, 120	7.58 9.39	2.11, 2.40
		1550	0.33 0.28		
S. Qin et al., [47]	Pancharatnam-Berry phase	Sb_2S_3	15.41, 20.38	60.08 55.31	0.920 1.083
		1310	0.714 0.608		
A. Afridi et al., [48]	Phase shift	PDMS	600 700	69.5 66.5	-
		632	0.24~		
M. Bosch et al., [49]	Phase delay	Liquid crystal	4500 9000	12.1 13.6	17.6 10.4
		800	0.08 0.04		
X. Yin et al., [50]	Geometric phase	GST-326	500 1000	10 5	-
		3100	0.5 0.8		
This work	Amplitude modulation	VO_2	3 6	9.31 13.47	0.341 0.250
		660	1.52 1.70		

2.3. Conclusion

Novel thermo-optically focus-switchable Fresnel zone plates based on phase-change metafilms are designed and analyzed at a visible wavelength (660 nm). By virtue of the large thermo-optic response of vanadium dioxide (VO_2) thin film, a phase-change material, four different plasmonic phase-change absorbers are numerically designed as actively tunable Gires-Tournois Al-VO_2 metafilms in two and three dimensions. The designed phase-change metafilm unit cells are used as the building blocks of actively focus-switchable Fresnel zone plates with strong focus switching contrast (40%, 83%) and high numerical apertures (1.52, 1.70). The Fresnel zone plates designed in two and three dimensions work as cylindrical and spherical lenses in reflection type, respectively. The coupling between the thermo-optic effect of VO_2 and localized plasmonic resonances in the Al nanostructures offer a large degree of freedom in design and high-contrast focus-switching performance based on largely tunable absorption resonances. The proposed method may have great potential in photothermal and electrothermal active optical devices for nonlinear optics, microscopy, 3D scanning, optical trapping, and holographic displays over a wide spectral range including the visible and infrared regimes.

Chapter 3 Multi-objective optimization of dynamic VO_2 metagratings: strong broadband modulation of transmittance for unpolarized light

3.1 Introduction

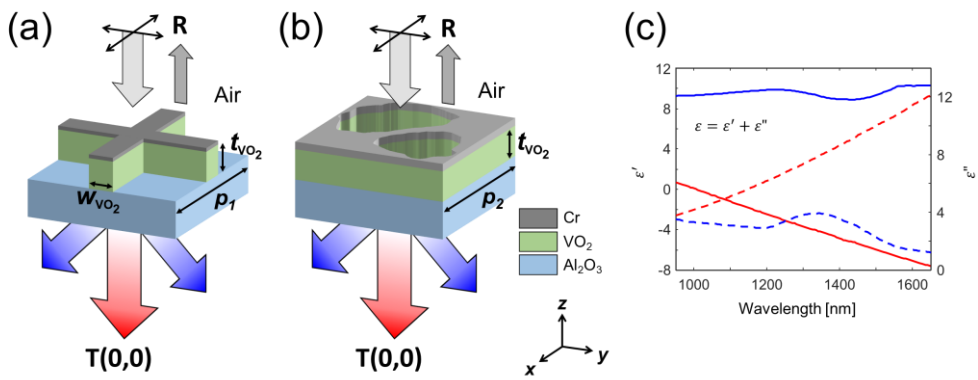

Figure 3.1 Schematics of the diffractive VO_2 (a) fishnet and (b) freeform metagrating for broadband transmittance modulation of unpolarized light incident. (c) Measured permittivity of VO_2 film.

Over the last decade, the field of metasurface optics, meta-optics, has grown rapidly for various unprecedented technological advantages over the traditional optical elements based on refraction and diffraction of light [51, 52]. In particular, myriads of optical metasurfaces, consisting of densely arranged nanostructured high-index (dielectric/metallic) nanoantennas on transparent substrates, have been developed for performing various wavefront modulation applications in the free space with high efficiency, crosstalk reduction, small form factor, light weight, and polarization-dependent multi-functionality [53, 54]. However, most of progressive

results on optical metasurfaces have been focused on passive meta-optic elements such as lens [12], hologram [55], and deflector [56] without post-fabrication tunability of optical functions.

When it comes to dynamic metasurfaces of which optical functions can be tuned according to the change of external control stimuli, there have been a variety of research on actively tunable metasurface platforms such as the configurations incorporating liquid crystals [57-59], transparent conducting oxides [61, 62], electro-chemical materials [58-72], electro-mechanical systems [27-28], and phase-change materials [69-72] with nanostructured metasurfaces [22-26]. Among those, phase-change materials have received much attention for their relatively large thermo-optic tunablity of dielectric functions over the broad optical wavelength range (from the visible to the infrared), despite the disadvantage of considerable intrinsic absorption loss [23, 69].

Vanadium dioxide, VO_2, is one of the representative phase-change materials, which shows the thermally driven reconfigurable insulator-to-metal transition (IMT) around the critical temperature of 68 ℃ [23]. The IMT induces large thermal tunability of dielectric function as well as electrical conductivity [23] so that many metasurface modulators employing VO_2 thin film [26-30, 72] have been reported. In particular, VO_2 based metasurface modulators for free space optical beams hold great potential for display [73], sensing [74], smart window [75], and optical communication [76] owing to their relatively low phase-change temperature and capability of fast repeated switching [77].

Among many kinds of modulation goals, transmittance modulation at the telecommunication band can find fundamental roles in the abovementioned applications. In 2018, we reported previous work exploiting diffractive VO_2 metagrating for broadband transmittance modulation [23]. The modulation mechanism of the metagrating is to combine dielectric-to-plasmonic transition effect at the telecommunication wavelengths with tunable vertical waveguiding in VO_2 nanoridges. However, as the previously reported device can only modulate transverse-electrically polarized light, novel design of polarization-independent modulation with multi-objective performance optimization is required considering potential practical use.

In this chapter, two different types of adjoint-optimized diffractive VO_2 metagratings aiming for broadband transmittance modulation of arbitrarily polarized light are proposed as shown in Figure 3.1(a) and 3.1(b), theoretically analyzed, and experimentally verified. The rest parts of the papers are organized as follows. First, our ideas and concepts are suggested. Then, optimization results and theoretical analysis are provided. Third, experimental results are discussed. And at last, the chapter ends with the conclusion including the summary of our work and perspective.

3.2 Principles of VO_2 metagrating modulator

3.2.1 Material properties and concepts

VO_2 film is of particular interest due to its large thermo-optic tunability of dielectric function, particularly in the infrared. The 340-nm thick VO_2 film is deposited on a substrate using a conventional pulse laser deposition (PLD) system (LAMBDA PHYSIK, COMPEX 205) with a KrF laser operating at 248 nm. To investigate the dielectric function, a spectroscopic ellipsometer (J. A. Woollam V-VASE) is being used with a thermocouple and an electrical heater. The dielectric function in the infrared region exhibits variation depending on the phase of VO_2, as shown in Figure 1(c). Specifically, in the infrared range above 1000 nm wavelength, there is a clear transition observed in the real part of the dielectric function as the phase of VO_2 changes. This transition is characterized by a change from a positive value to a negative value. When unpolarized light is incident on the sample, it is effectively guided within the insulating VO_2 nanostructure. However, in the metallic phase, the VO_2 structure becomes opaque to light, leading to a significant suppression of the interaction between light and VO_2.

Figure 3.1(a) and (b) show schematic diagrams of two types of VO_2 diffraction metagrating designed for broadband transmittance modulation of light using this phenomenon. Both structures exhibit a diagonally symmetrical shape to ensure isotropic operation. When light with unpolarized light illuminates the VO_2 metagrating in the insulating phase, it undergoes a division. A portion of the light is guided within the VO_2 metagrating, while the rest is redirected into the air. As the guided light passes through the VO_2 material, its phase changes, resulting in a

phase difference compared to the redirected light in the air. This phase difference leads to diffraction into orders other than the 0th order, to be in the off-state. On the other hand, when light is incident on the VO_2 in the metallic phase, light is rarely guided into the VO_2 metagrating, and the majority of the light is detour into the air. Since the detour light in the air maintains the same phase, it transmits through the 0th order in the on-state.

To enhance the efficiency of transmitted light and achieve a significant modulation depth, the grating's period is carefully chosen to prevent diffraction other than the 0th order on the incident side (air) while allowing for diffraction on the emitting side (Al_2O_3 substrate). The grating period is determined within the range of $\lambda/n_{substrate} < p < \lambda$, where λ represents the wavelength. To effectively implement this phenomenon, numerical analysis optimization was employed to determine the optimal structure. By conducting numerical simulations, we were able to optimize the geometric parameters of the grating structure to maximize the desired effects and the performance of broadband thermo-optic transmission modulation.

3.2.1 Numerical optimization of metagratings

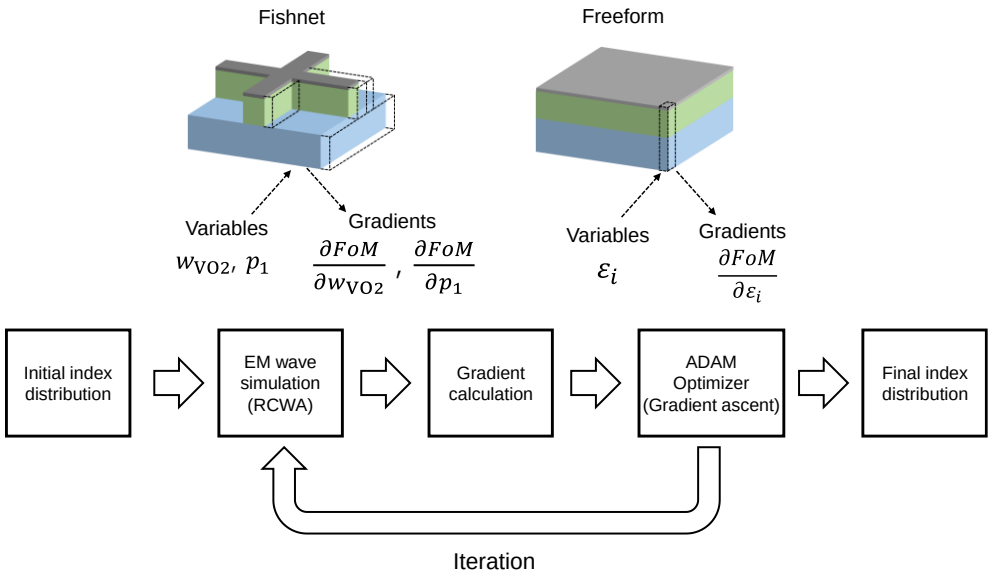

Figure 3.2 Schematic diagram of the optimization process

The optimization process of the proposed structure follows the flow shown in Figure 3.6. The Figure of Merit (FoM) is defined as a linear combination of modulation depth at three wavelengths (1400 nm, 1500 nm, 1600 nm). For the fishnet VO_2 metagrating, electromagnetic (EM) simulations are performed with arbitrary initial values for the width and period to optimize the design. Then, the gradient of the FoM is computed, and gradient ascent is performed using the ADAM optimizer to maximize the FoM [78]. As a result, the optimized values for the metagrating period (p) and the width of the VO_2 ridge (w_{VO2}) are found to be 1234 nm and 359 nm, respectively.

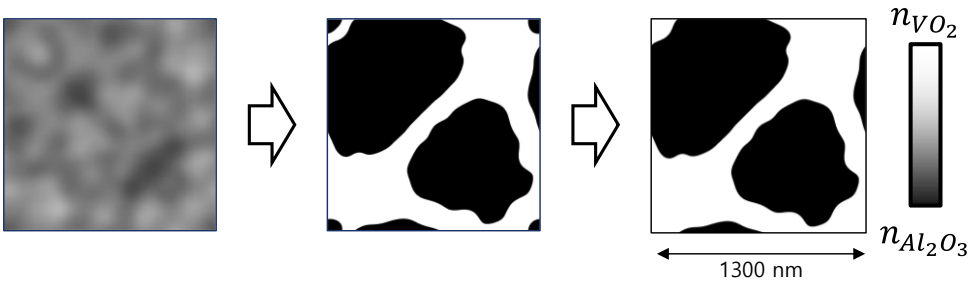

Figure 3.3 Optimized freeform VO_2 metagrating

For the freeform metagrating, the optimization is conducted pixel by pixel with a size of 1 nm × 1 nm by varying the permittivity through the same process. In consideration of fabrication feasibility, binarization is applied to restrict the permittivity values to either air or VO_2, and Gaussian blurring is employed to remove small structures that are not realizable in the fabrication process. The optimized unit cell of the freeform VO_2 metagrating is designed as shown in Figure 3.3 with period of 1300 nm.

3.2.2 Theoretical analysis

Figure 3.2 presents the electric field intensity of the unit cell to theoretically validate the two types of metagratings discussed in section 2.2. When a plane wave of unpolarized with a wavelength of 1500 nm is incident perpendicularly to the air side of the unit cell, the emitted light from the Al_2O_3 substrate undergoes significant tuning as the phase of VO_2 changes. In the insulating phase, both the fishnet and freeform VO_2 modulators emit light with diffraction orders other than the 0th order, as shown in Figures 3.4(a) and 3.4(c) respectively. Conversely, in the metallic phase, strong emission of light in the $-z$ direction, specifically the 0th order, is observed in Figures 3.4(b) and 3.4(d). Notably, the asymmetrical structure of the freeform modulator leads to the emission of asymmetrical diffraction orders for all phases of VO_2, as shown in Figures 3.4(c) and 3.4(d). Figure 3.3 shows the 3D far-field results of the fishnet (Figures 3.5(a) and 3.5(b)) and freeform (Figures 3.5(c) and 3.5(d)) unit cells. As discussed previously, both the fishnet and freeform VO2 metagratings emit light with diffraction orders other than the zeroth order, as indicated in Figures 3.5(a) and 3.5(c) for the insulating phase. In contrast, in the metallic phase, strong emission is observed in the -z direction, particularly in the 0th order, as seen in Figures 3.5(b) and 3.5(d). Particularly, the freeform metagrating's asymmetric structure results in emission characterized by highly asymmetric diffraction orders in the insulating phase, as shown in Figure 3.5(c).

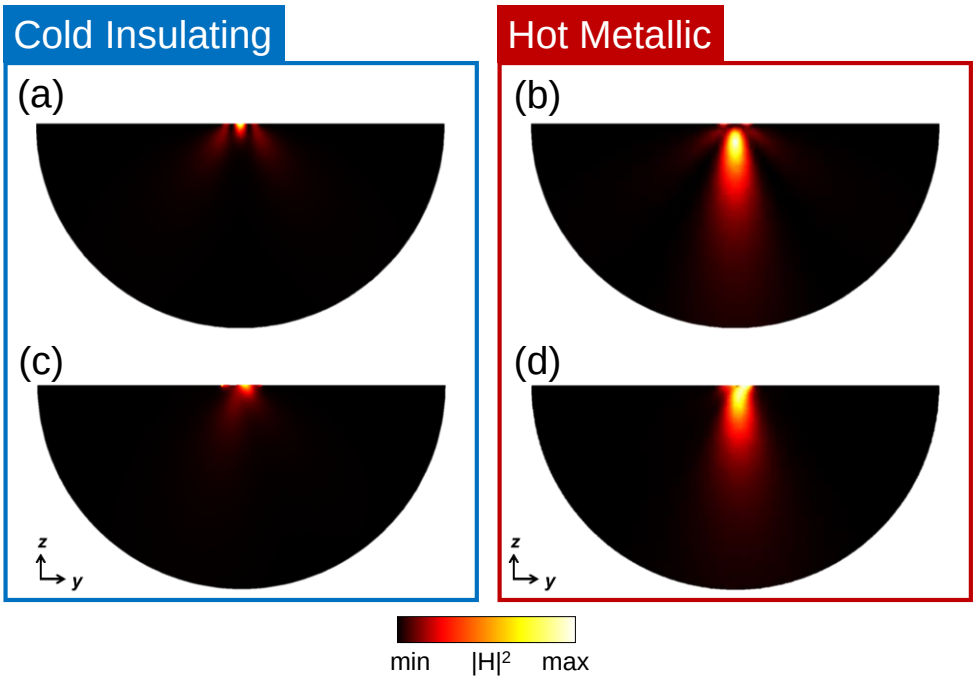

Figure 3.4 Normalized transmitted electric field intensity distribution of unit cell of (a), (b) fishnet and (c), (d) freeform VO_2 metagrating modulator at the insulating and metallic phases, respectively. The wavelength is set to be 1500 nm.

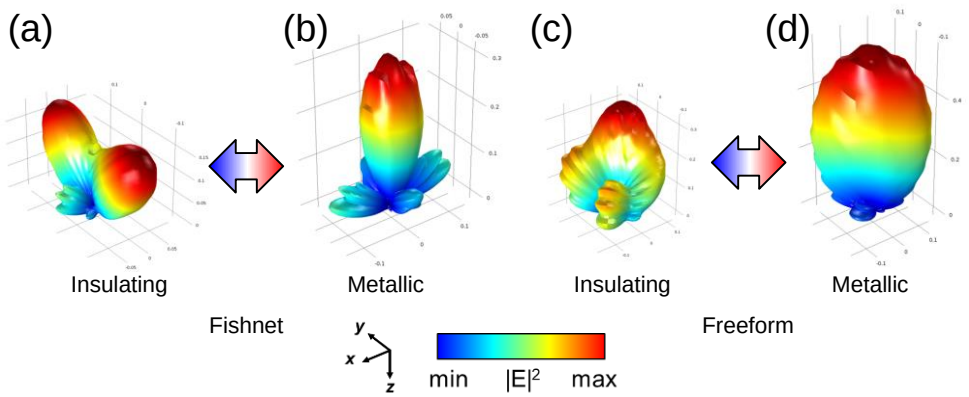

Figure 3.5 The 3-dimensional far-field of unit cell of (a), (b) fishnet and (c), (d) freeform VO_2 metagrating modulator at the insulating and metallic phases, respectively. The wavelength is set to be 1500 nm.

Figures 3.6(a) and 3.6(b) demonstrate the transmittance and reflectance characteristics of Fishnet VO_2 metagrating unit cells arranged periodically with a period of 1234 nm. These figures reveal the behavior of each diffraction order in both the insulating and metallic phases. Notably, the modulation of the 0th order transmission is highly influenced by the phase change, surpassing the impact on other diffraction orders. In the insulating phase, the magnetic field intensity in the xy-plane illustrates that incident light is divided into two components: light coupled into VO_2 and light detour into the air, as shown in Figure 3.6(c). The coupled light in VO_2 exhibits a phase delay and phase difference relative to the redirected light, resulting in transmission through a diffraction order other than the 0th order. This phenomenon is clearly observed in the E_x field distribution shown in Figure 3.6(e). Conversely, in the metallic phase, the coupling of light into VO_2 is minimal across all wavelengths, with most of the light bypassing through the air, as shown in Figure 3.6(d). Consequently, the transmitted light through the metagrating predominantly occurs in the 0th order with a similar phase (Figure 3.6(f)). The absorption loss ($A = 1 - T_{total} - R$) remains uniformly around 0.6 throughout a wide NIR band, irrespective of the phase change in VO_2. Therefore, this confirms that the modulation of the 0th order transmittance occurs by converting the light coupled into VO_2 due to the phase change into a different diffraction order, rather than modulating it through absorption within VO_2.

Similarly, when the unit cells of freeform VO_2 metagrating are arranged with a period of 1300 nm, Figures 3.7(a) and 3.7(b) exhibit the transmittance and reflectance profiles for each diffraction order in both the insulating and metallic

phases. Again, the modulation of the 0th order transmission is highly influenced by the phase change rather than other diffraction orders. In the insulating phase, the magnetic field intensity in the *xy*-plane demonstrates the division of incident light into two components: light coupled into VO_2 and light diverted into the air, as illustrated in Figure 3.7(c). The coupled light in VO_2 experiences a phase delay and phase difference compared to the diverted light, resulting in transmission through a diffraction order other than the 0th order. This behavior is clearly observed in the E_x field distribution depicted in Figure 3.7(e). In the metallic phase, light coupling into VO_2 is minimal for all wavelengths, with the majority of the light bypassing through the air, as shown in Figure 3.7(d). Consequently, the transmitted light through the metagrating predominantly occurs in the 0th order with a consistent phase (Figure 3.7(f)). The absorption loss remains approximately 0.7 uniformly across a wide NIR band, regardless of the phase change in VO_2. In summary, the modulation of the 0th order transmittance occurs by converting the light coupled into VO_2 due to the phase change into a different diffraction order. The fishnet and freeform VO_2 metagrating modulators demonstrate the effectiveness of this principle.

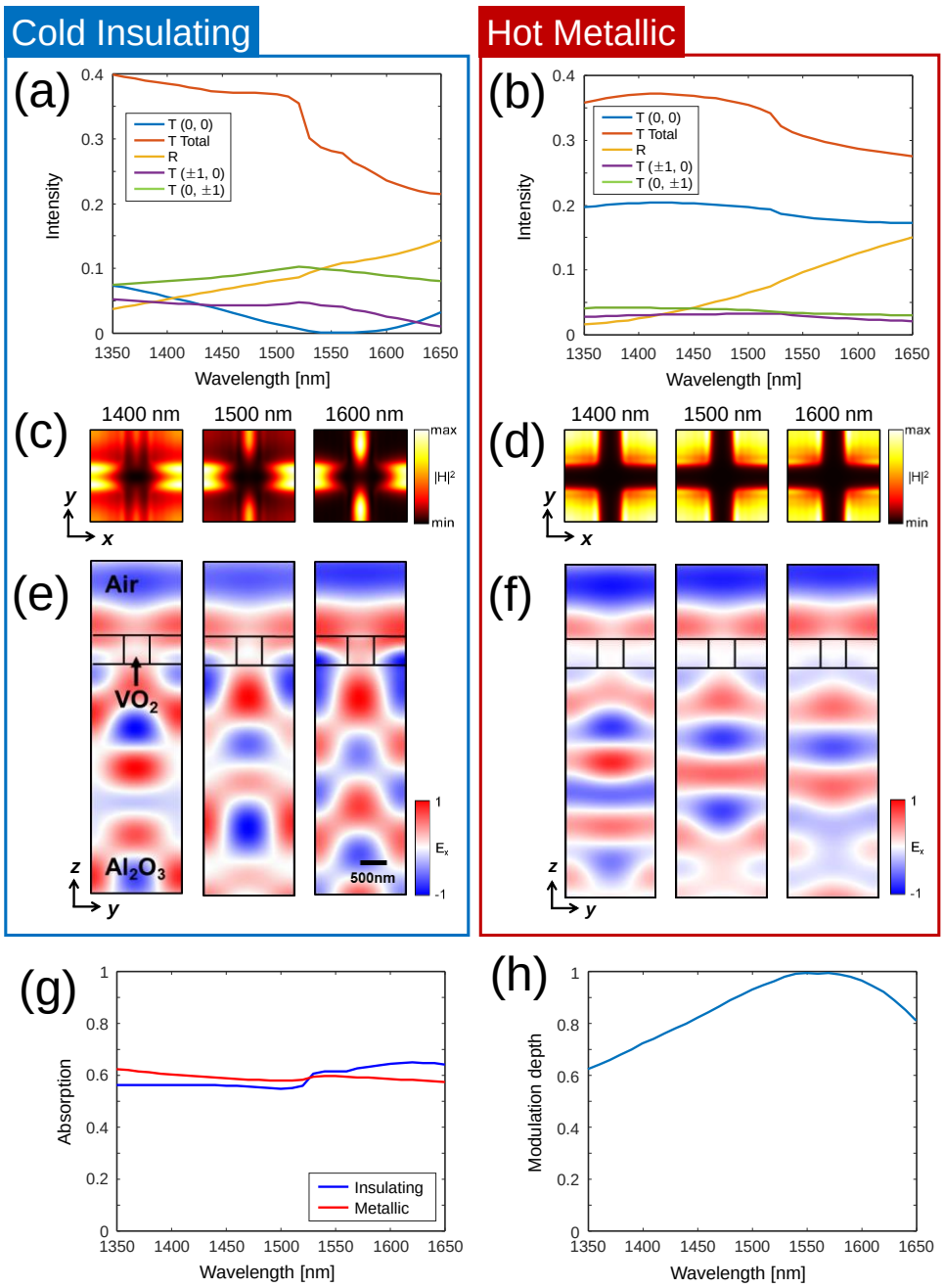

Figure 3.6 Numerical transmittance spectra of the fishnet VO_2 metagrating modulator in the (a) insulating and (b) metallic phase. Normalized profile of (c), (d) magnetic field intensity on *xy*-plane and (e), (f) E_x field on *yz*-plane at each phase. (g) Broadband absorption and (h) modulation depth spectra

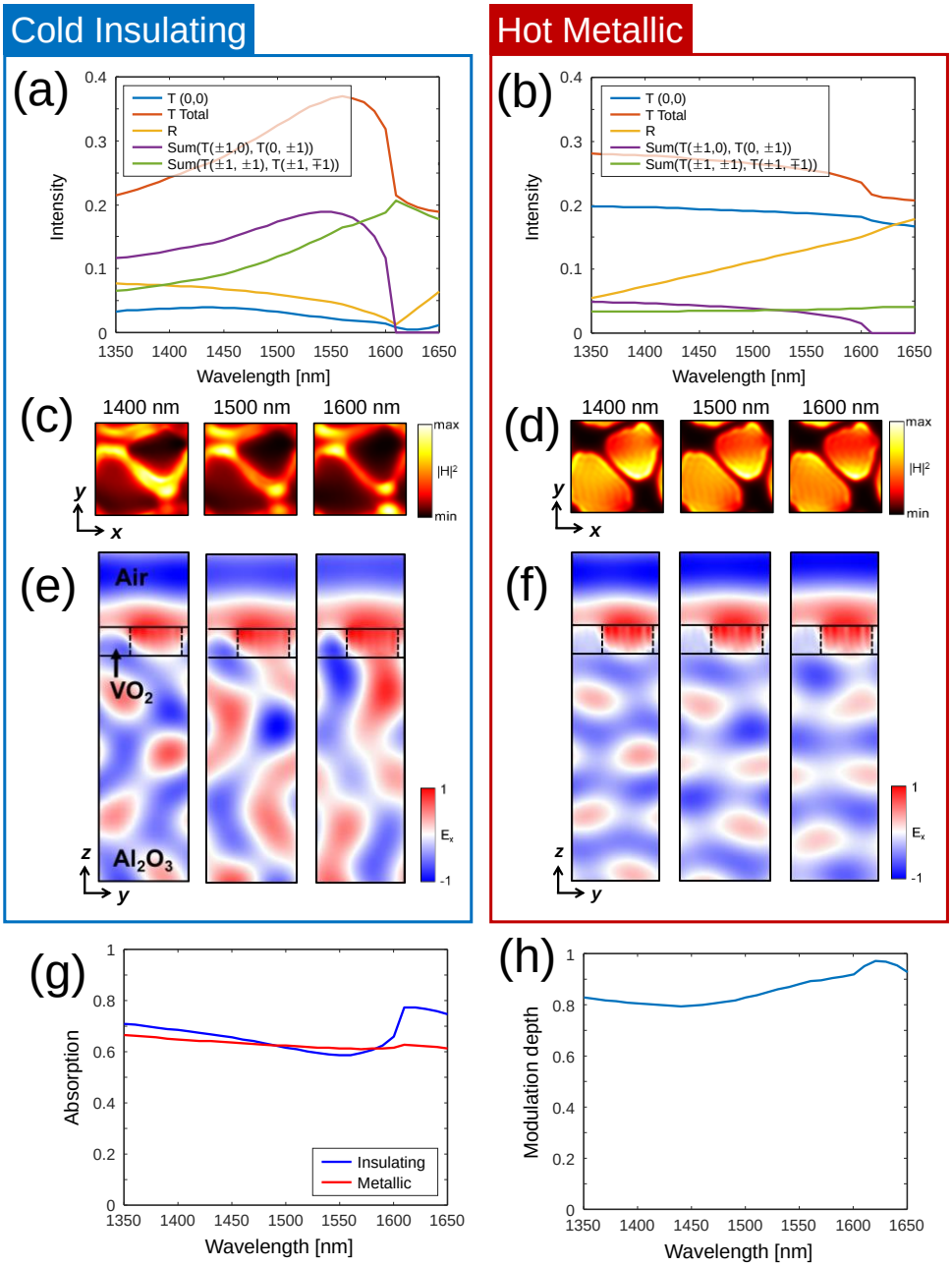

Figure 3.7 Numerical transmittance spectra of the freeform VO_2 metagrating modulator in the (a) insulating and (b) metallic phase. Normalized profile of (c), (d) E_x field on *yz* plane and (e), (f) magnetic field intensity on *xy* plane at each phase. (g) Broadband absorption and (h) modulation depth spectra

Furthermore, for quantitative analysis of the modulation performance, the modulation depth is also numerically investigated in Figure 3.6(h) and 3.7(h), respectively. Both structures of the VO_2 metagrating demonstrated approximately 20% transmittance and an average modulation depth of 0.85 in the on-state. Notably, the freeform metagrating exhibited a standard deviation of modulation depth of 0.058, which is narrower than that of the fishnet metagrating with a standard deviation of 0.119.

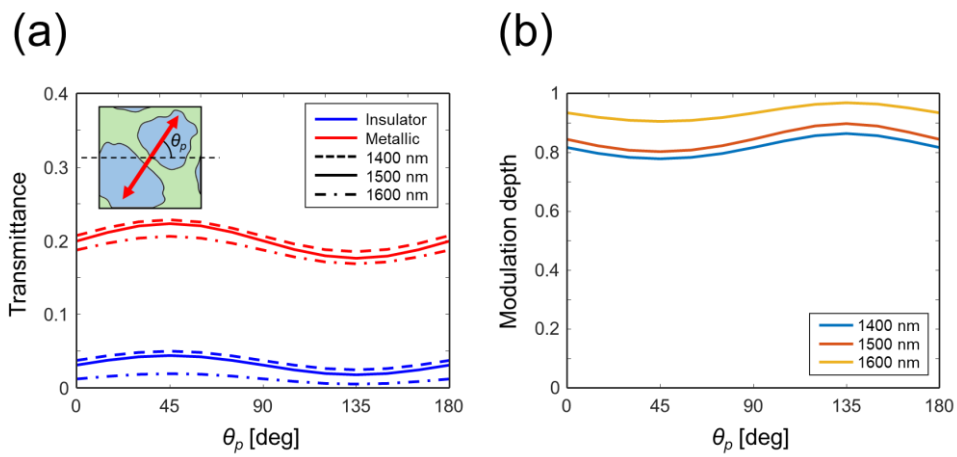

Figure 3.8 (a) Transmittance and (b) modulation depth according to the polarization angle of linearly polarized incident light.

The freeform VO_2 metagrating has a diagonal symmetric structure, leading to varying transmittance depending on the angle of incident light polarization, as shown in Figure 3.8 (a). The blue and red curves represent the behavior of VO_2 in the insulator and metallic phases, respectively. When the polarization angle, θ_p, is at 0º or 90º (corresponding to *x*-pol and *y*-pol), the transmittance of the 0th order mode remains consistent across wavelengths 1400 nm, 1500 nm, and 1600 nm,

similar to design. However, at θ_p = 45º, the transmittance is approximately 2% higher for incident light with *x* - pol, regardless of VO_2's phase and the wavelength of the incident light. In constrast, at θ_p = 135º, the transmittance decreases by approximately 2% for incident light with *x*-pol, regardless of VO_2's phase and the wavelength of the incident light. The modulation depth (Figure 3.8 (b)) exceeds 0.78 in all cases, indicating that the designed freeform VO_2 metagrating operates effectively with unpolarized incident light.

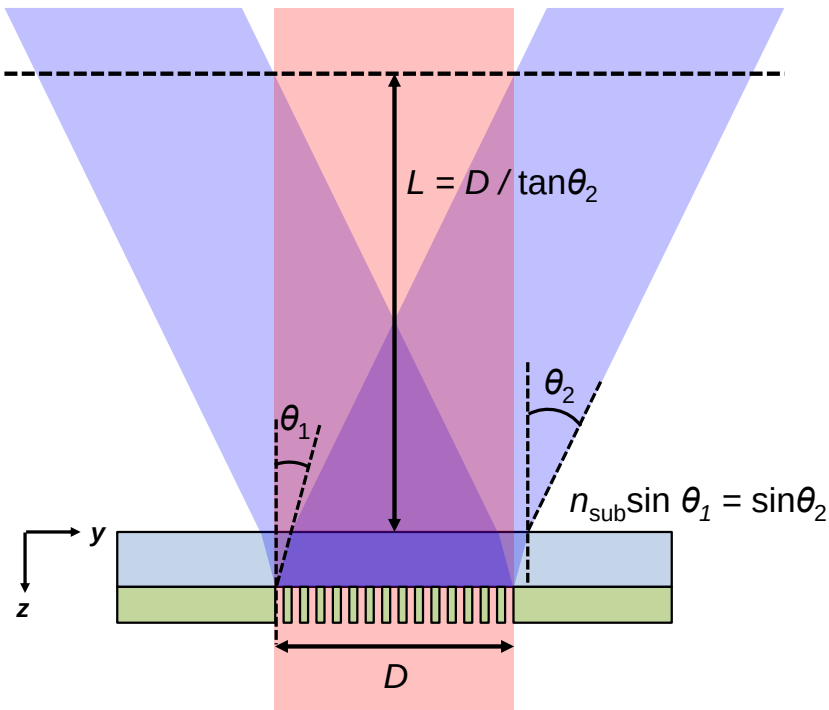

Figure 3.9 The light transmitted through the VO_2 metagratings

The light transmitted through the VO_2 metagratings is separated into the 0th order and other orders, as shown in Figure 3.9. The light that enters the VO_2 metagrating from the air is emitted through the Al_2O_3 substrate. Upon exiting the

substrate and propagating into the air, the emitted light undergoes refraction according to Snell's law, with $\theta_2 = \sin^{-1}(n_{sub} \cdot \sin\theta_1)$, where θ_1 represents the angle of the diffracted light in the insulating phase of VO_2. Given a sample size of D, the distance at which the diffracted light becomes completely separated from the zeroth order is calculated as $L = D/\tan\theta_2$. The smallest value of θ_1 occurs when the freeform VO_2 metagrating is in the insulating phase and allows transmission of light diffracted into the (1, 1) order. In this case, θ_1 is 15 ˚. Assuming a sample size of 100 μm, the distance at which the 0th order and other orders are fully separated amounts to approximately 196 μm. This distance is smaller than the typical thickness of a sapphire wafer.

3.3 Experimental demonstration

3.3.1 Fabrication of metagrating

To validate the proposed transmission modulator, a VO_2 metagrating sample is manufactured using a three-step fabrication process. Initially, a 340 nm-thick VO_2 film is deposited on a substrate. Then, a 10 nm-thick chromium (Cr) protection hard mask is applied onto the VO_2 film using e-beam evaporation (Korea Vacuum Tech, KVE-3004). The purpose of the Cr deposition is to reduce the tapering effect caused by ion beam milling and minimize the stoichiometric effect of Ga+ ions on the VO_2 film.

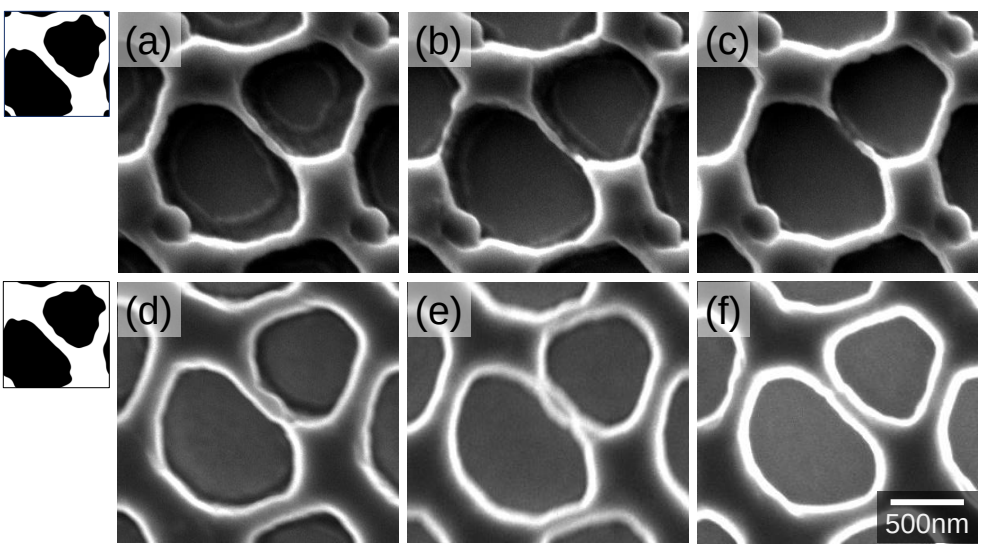

Figure 3.10 SEM images of unit cells of freeform VO_2 metagrating according to the (a)-(c) presence or (d)-(f) absence of nanohole and the milling depth (z) of FIB (a) z = 1100 nm, (b) z = 1200 nm, (c) z = 1300 nm, (d) z = 1300 nm, (e) z = 1400 nm and (f) z = 1500 nm

As shown in Figure 3.10 (a)-(c), holes with widths below x nm do not form properly. Therefore, as shown in Figure 3.10 (d)-(f), the sample was fabricated excluding the smallest nanoholes. The impact of the nanohole presence is shown in Figure 3.9. It was observed that nanoholes have minimal effect on the H-field distribution. Furthermore, from the transmittance (Figure 3.11(a)) and modulation depth (Figure 3.11(b)), it can be seen that the performance degradation due to the removal of nanoholes is negligible. Therefore, for ease of fabrication, a structure without nanoholes was chosen.

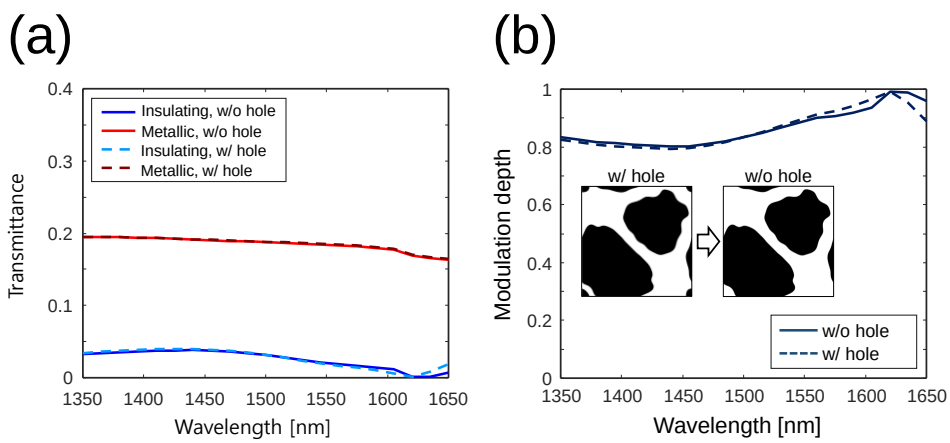

Figure 3.11 Spectra changes in (a) transmittance and (b) modulation depth according to the presence or absence of nanohole.

During the fabrication process using ion beam, the fabricated sample tends to be larger than the desired size. Therefore, the pattern input to the focused ion beam (FIB) was designed to be 100 nm smaller than the desired sample size to achieve the desired size. Additionally, the milling depth (z) of the input pattern was adjusted to increase the ion beam irradiation time, ensuring that the VO_2 layer is fully milled. This process can be seen in Figure 3.10, ultimately resulting in the outcome shown in Figure 3.10 (f).

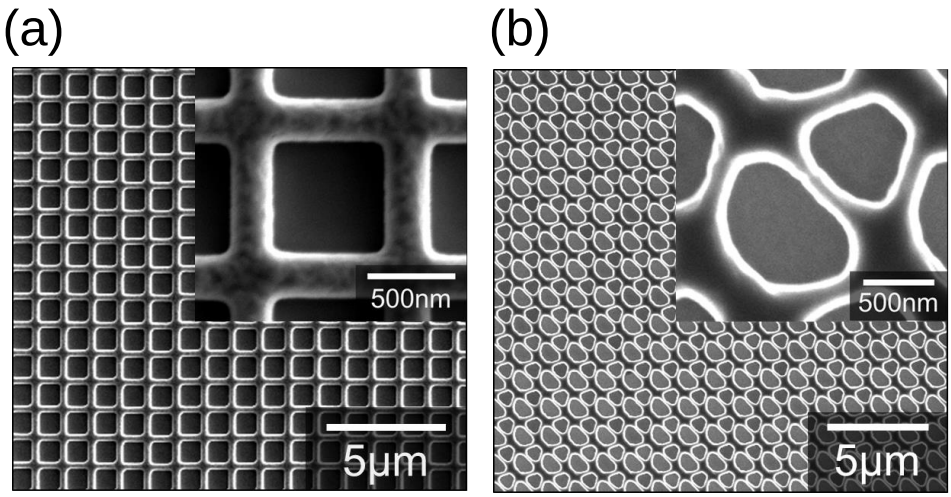

Figure 3.12 Scanning electron microscope images of the fabricated (a) fishnet and (b) freeform VO_2 metagrating. The inset image shows that unit cell of metagratings respectively.

In the final step, two distinct types of VO_2 metagratings are patterned by focused ion beam machine (FEI, Quanta 200 3D). The milling process involves 17 × 17 periodically arranged unitcells of the metagratings, resulting in the sample footprint about 20 μm × 20 μm. Figure 3.12 (a) and 3.12 (b) show scanning electron micrographs of the fabricated fishnet and freeform metagrating modulators, respectively.

3.3.1 Experimental results

The microscopic spectroscopy experiments are conducted with the varying temperature of the sample. A broadband white light source (YOKOGAWA, AQ4305) is focused onto the sample using an objective lens. To exclusively measure the transmission of the 0th order, the incident light is directed onto the sample substrate, and the emitted light in the air layer (where other diffraction orders are absent) is collected using another objective lens. To further isolate the desired transmission, a field-stop iris is utilized to block any unwanted light. The transmitted signal is then captured by an optical fiber through a beam collimator and subsequently analyzed using an optical spectrum analyzer (YOKOGAWA, AQ6370D). This setup ensures that only the light transmitted through the sample, specifically the 0th order is measured and analyzed. Figure 13 shows the setup for measuring the transmission spectrum of the 0th order. The temperature of the fabricated sample is controlled using a Peltier device stage (Linkam PE120).

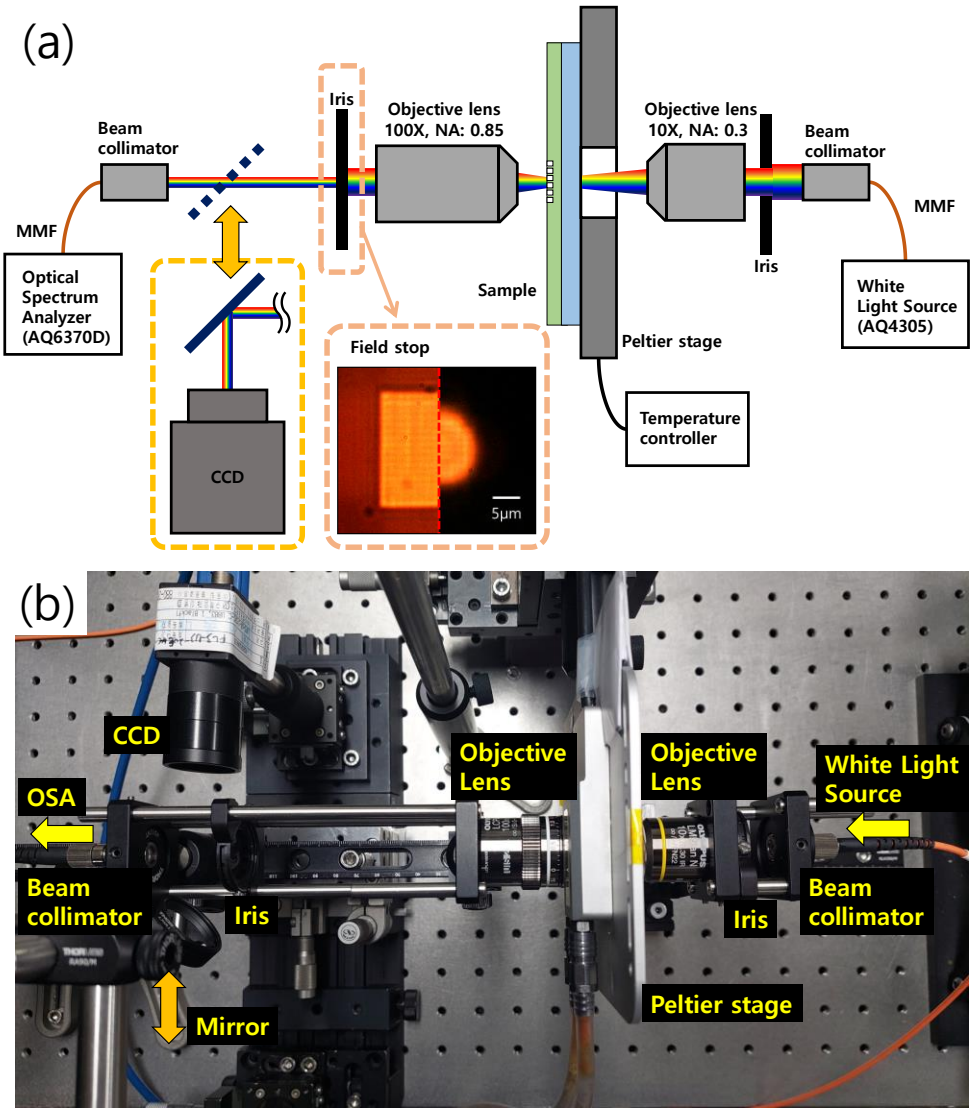

Figure 3.13 Schematic of the experimental setup for the 0th order transmittance measurement

Figure 3.14 shows the measured transmission spectrum, which exhibits notable levels of noise. The presence of this noise is attributed to the optical components with different bandwidths. Specifically, the objective lens and the optical spectrum analyzer operate within the ranges of 700-1300 nm and 800-1700 nm, respectively. Additionally, the inclusion of a filtering component, such as a

field stop iris, contributes to a reduction in the power of the incident beam. Consequently, the power spectrum of the input source experiences a significant decrease, particularly in the long-wavelength region ranging from 1350 nm to 1650 nm, which corresponds to the targeted range for the measurement.

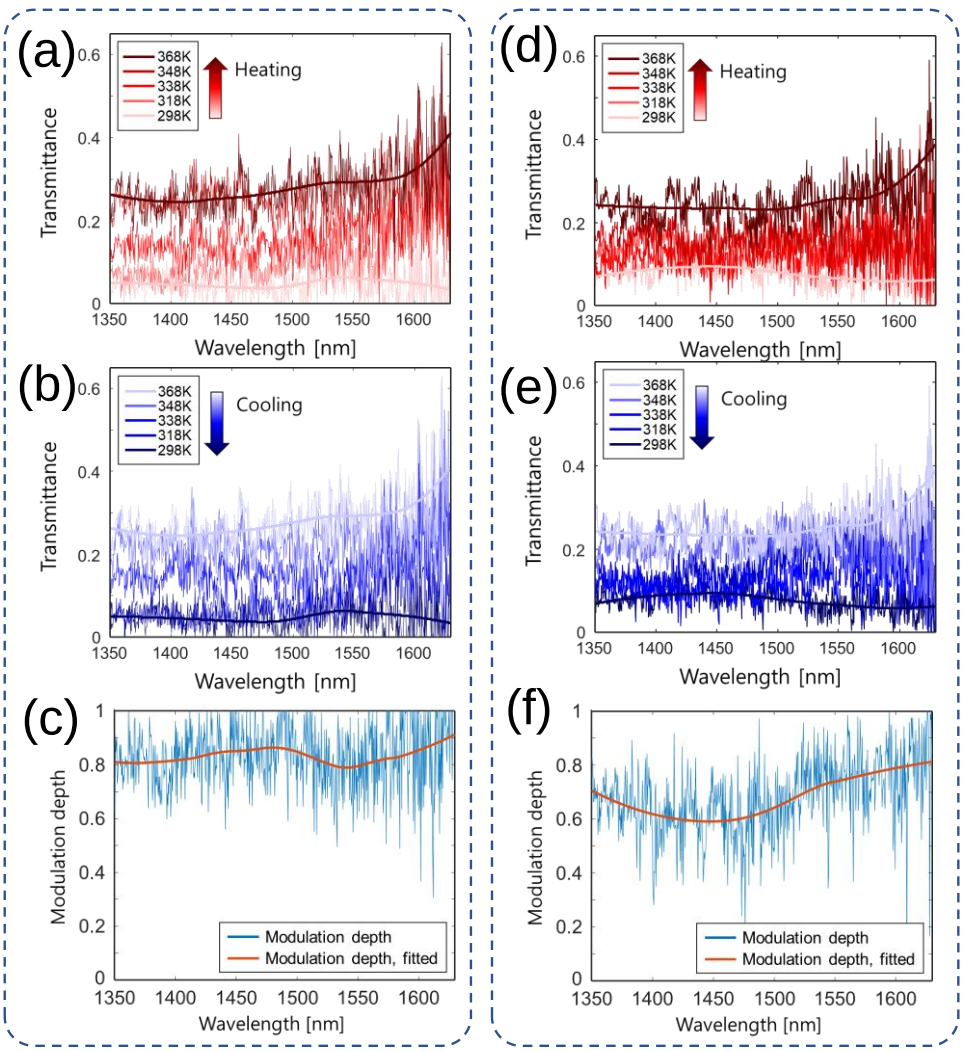

Figure 3.14 The measured 0th order transmittance spectra in (a-c) fishnet and (d-f) freeform VO_2 metagrating. (a), (d) heating and (b), (e) cooling processes respectively. (c), (f) calculated modulation depth and linearly fitted line.

In Figures 3.14(a) and 3.14(b), the measured transmittance spectra of a fishnet VO_2 metagrating are displayed for heating and cooling processes, respectively. These spectra exhibit a gradual change in transmittance corresponding to the variation in temperature. In Figure 3.14(c), the modulation depth is calculated using the measured values at 298 K (the insulating phase) and 368 K (the metallic phase). The measured modulation depth exhibits an average of 0.84 with a standard deviation of 0.048. This indicates a uniform and deep modulation depth a broad bandwidth in a good agreement with the simulation results.

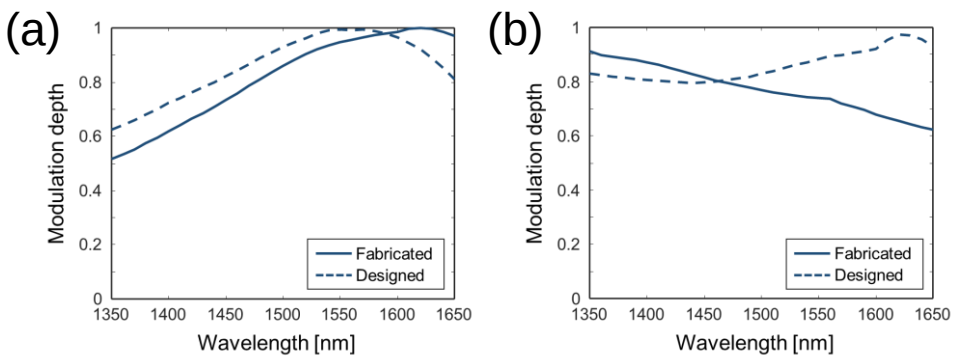

Figure 3.15 The simulated modulation depth of the (a) fishnet and (b) freeform VO_2 metagrating modulators, considering fabrication tolerances

Figure 3.15 shows the modulation depth for both the fabricated and designed metagratings, considering the geometric parameter. The impact of process errors on the modulation depth is more significant in the freeform (Figure 3.15 (b)) than in the fishnet (Figure 3.15(a)) VO_2 metagrating modulator. This discrepancy in modulation depth caused by fabrication tolerance is directly related to the performance disparity observed in Figures 3.14(c) and 3.14(f).

3.4 Conclusion

The novel multi-objective optimized metagrating devices are proposed and verified through the numerical and experimental studies. The on-state transmittance is around 0.3 for unpolarized in the wavelength-independen, while the average modulation depth is about 0.8. Additionally, the integration of a metallic thin film micro-heater could potentially enable rapid electrical modulation and pixel-by-pixel phase-change.

The author anticipates that the proposed device and concept will be fruitful for development of novel spatial light modulators, optical routers, and three-dimensional optical scanning sensors. The small pixel pitch and operation in the near-infrared (NIR) and infrared (IR) regimes make it particularly promising for these applications.

Chapter 4 Experimental study on electro-thermal modulation of VO_2 film structure

4.1 Introduction

Numerous studies have been conducted on the amplitude and phase modulation of VO_2 due to its thermo-optical properties, which exhibit a significant refractive index modulation factor [21-30]. However, the modulation speed associated with these thermo-optical properties is considerably slow. To address this limitation, researchers have undertaken various investigations into the electro-thermal-optical modulation properties of VO_2. While recent experimental studies by Jon Schuller's group [68] and Harry Atwater's group [22, 25] have reported on VO_2 metasurface devices capable of high-speed electro-thermal modulation, achieving high-speed modulation in the visible light band remains an ongoing challenge. Thus, this chapter presents experimental research findings aimed at achieving high-speed electro-thermal amplitude modulation in the visible-near infrared (NIR) band using VO_2.

4.2 Material properties and concepts

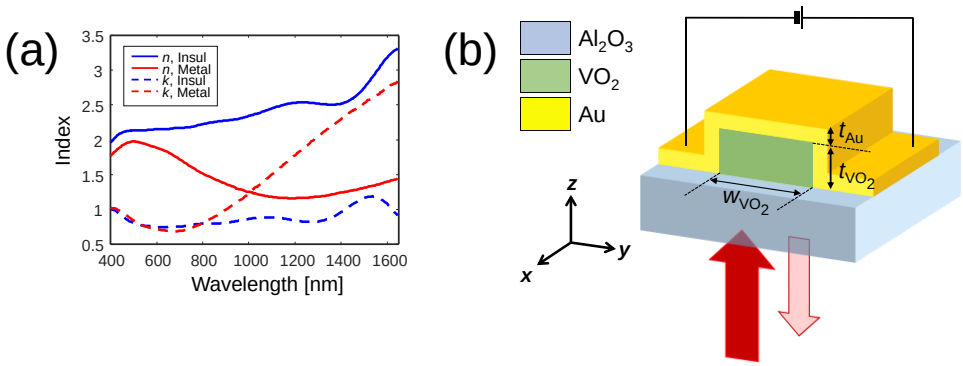

Figure 4.1 (a) Measured permittivity of VO_2 film. (b) Schemetic of VO_2 nanostructure

In this chapter, the VO_2 film used has a thickness of 314 nm and is deposited on an Al_2O_3 substrate using the PLD method. The refractive index of the VO_2 film is depicted in Figure 4.1(a). An electrical connection is established by employing a gold electrode that is attached to the VO_2 film. By applying an electrical signal, the reflectance change is measured when incident light, with any polarization towards the substrate, interacts with the VO_2 film. The reflectance change corresponds to the transition of the VO_2 film from the insulating phase to the metallic phase, driven by the electrical signal. Various electric signals, both Direct Current (DC) and Alternating Current (AC), are applied to investigate the modulation phenomenon exhibited by VO_2.

.

4.3 Experimental demonstration of high-speed electro-thermal amplitude modulation

Figure 4.2 presents the process flow for fabricating the VO_2 film with Au electrical-heating patch attached. First, a 314 nm-thick VO_2 film is deposited using the conventional PLD technique. Subsequently, negative photoresist (PR 1) is applied for patterning the VO_2 (width of VO_2 = 30 μm), followed by the removal of PR 1. A positive photoresist (PR 2) is then applied to the patterned VO_2 sample, enabling the electrical-heating patch patterning process. A 100 nm-thick Au film is deposited onto the patterned sample using an e-beam evaporator (Korea Vacuum Tech, KVE-3004). The removal of PR 2 completes the fabrication of the Au electrical-heating patch on the VO_2.

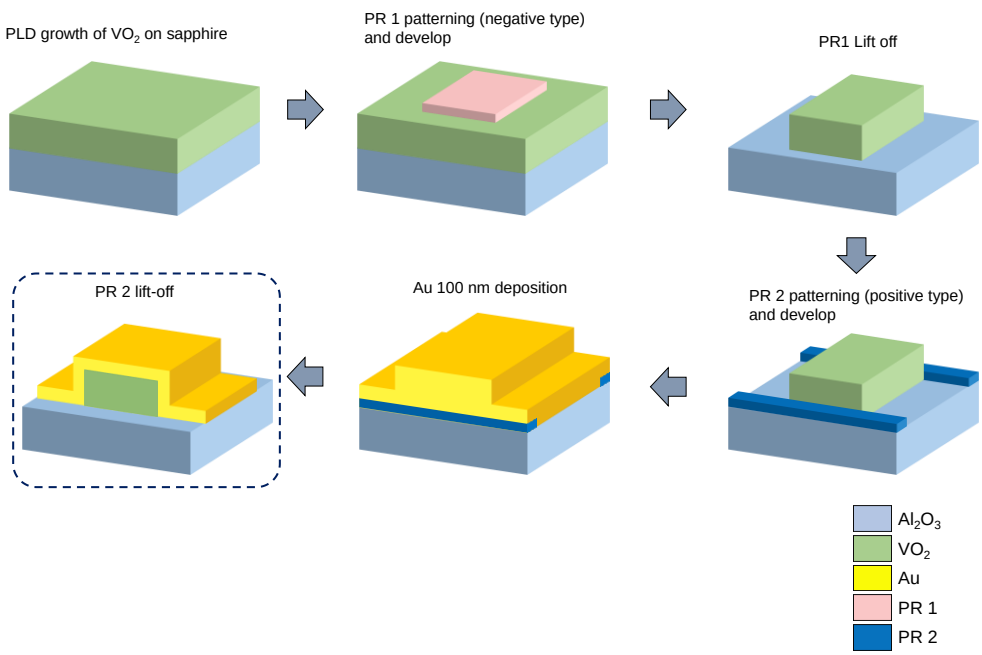

Figure 4.2 Schematic diagram of manufacturing process of VO_2 film with Au electrical-heating patch attached

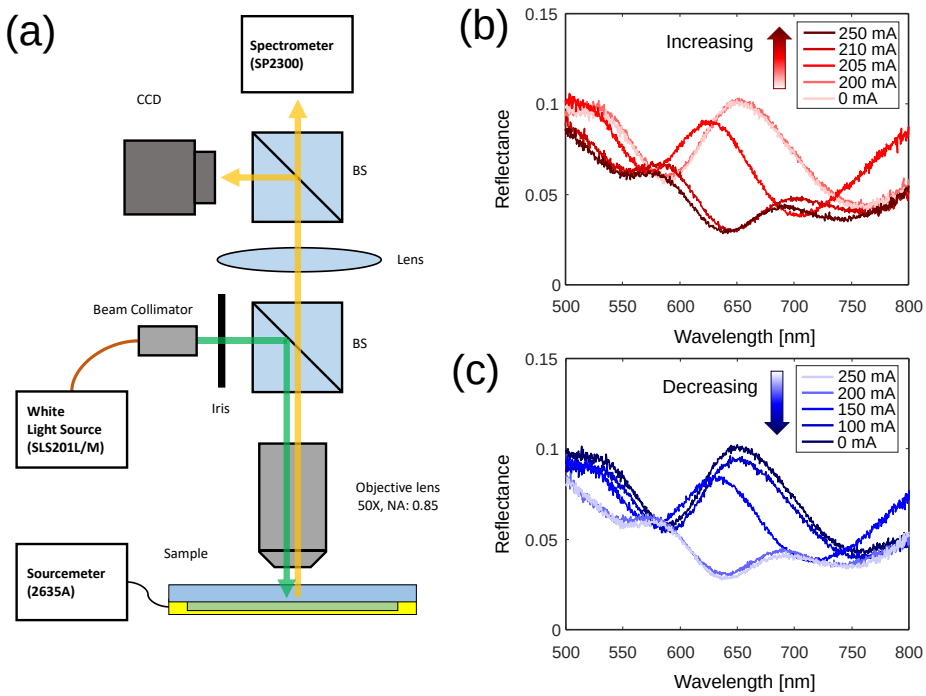

Figure 4.3 DC experiment setup and results (a) Schematic of the optical setup for electrically tuning the spectra response of the VO_2 film. Measured reflection spectra for various intensities of electrical current applied. (a) Increasing and (b) decreasing current, respectively

In Figure 4.3(a), the optical arrangement for evaluating the spectral response of an electrically controlled VO_2 film is presented. The light source used is a broadband white light, which is directed onto the sample through an objective lens. Subsequently, the reflected light is once again focused by the same objective lens, and a spectrometer (Princeton Instruments, Acton SP2300) captures a continuous spectrum across a wide range. Reflectance spectra were recorded for various levels of applied current. Figure 4.3(b) illustrates the reflection spectrum obtained when the current is increased, while Figure 4.3(c) depicts the spectrum for decreasing current. These graphs clearly indicate gradual changes in reflectance as the current is modified. Moreover, it is noteworthy that the phase transition occurs at different

current levels, with an increase at 205 mA and a decrease at 150 mA, showing the reconfigurable properties of VO_2.

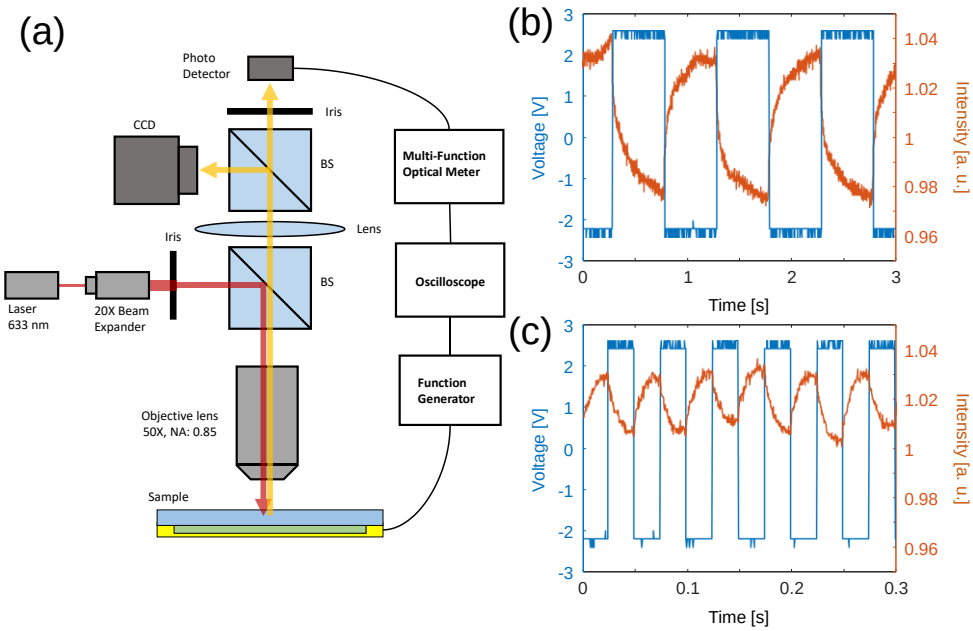

Figure 4.4 AC experiment setup and results (a) Schematic of the optical setup for the temporal response measurement of the VO_2 film (b) 1 Hz and (c) 20 Hz 4.5 V_{pp} pulse voltage input, measured at a wavelength 633 nm.

Figure 4.4(a) illustrates the experimental setup designed to measure the modulation of reflectance when an AC electrical signal is applied to the VO_2 film. The function generator is responsible for changing the frequency of the pulse signal, which has a peak-to-peak voltage of 4.5V, and feeding it as an electrical signal to the gold electrical-heating patch. The reflected light intensity from the sample is measured using a photo detector, and both the signal from the function generator and the measured light intensity are recorded using an oscilloscope. The measurement is conducted using light with a wavelength of 633 nm. Notably, when the pulse signal frequency is set at 20 Hz, the modulation size of the reflected light,

as detected by the photo detector, is observed to be half compared to when it is set at 1 Hz.

4.4 VO_2 extraordinary optical absorption grating

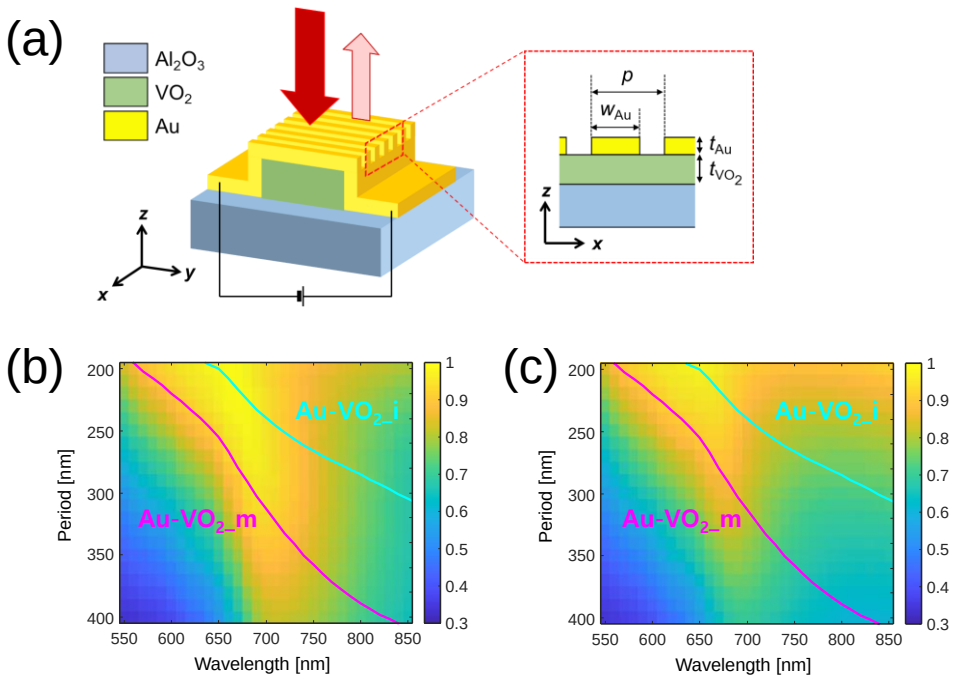

Figure 4.5 (a) Schematic diagram of the structure with gold nanobeams on VO_2 film with gold electrical-heating patch attached. Simulated absorption spectra according to the period of gold nanobeams at (b) insulating and (c) metallic phase of VO_2, respectively.

Surface plasmon polaritons (SPPs) are electromagnetic waves that are bound to an interface between a metal and dielectric layer and coupled to the collective oscillations of the free electrons in the metal [79, 80]. The modal characteristic of SPP wave propagation can be explained clearly by dispersion relation which originates from the continuity and momentum relation as follows.

$$k_{\mathrm{SPP}} = k_0\sqrt{\frac{\varepsilon_{\mathrm{VO_2}}\varepsilon_{\mathrm{Au}}}{\varepsilon_{\mathrm{VO_2}}+\varepsilon_{\mathrm{Au}}}} \tag{4.1}$$

The $\varepsilon_{\mathrm{Au}}$ represents the permittivity of gold, while $\varepsilon_{\mathrm{VO2}}$ represents the permittivity of VO_2. The k_0 represents the wavenumber in free space ($k_0 = w/c$).

here, as the permittivity of VO_2 changes with the insulator-to-metal transition (IMT), the conditions for SPP excitation also change.

To enhance the effectiveness of high-speed electrical amplitude modulation, a proposed method involves fabricating nanostructures on the gold electrical-heating patch that cover the VO_2 films. Figure 4.5(a) depicts the structure proposed, wherein a gold beam with a period (p) and width (w_{Au}) is positioned on the VO_2 film. By setting the thickness (t_{Au}) and spacing ($w_{Air} = p - w_{Au}$) of the gold beams at 80 nm each, the simulated absorption spectra based on the period of gold nanobeams are presented in Figure 4.5(b) and (c). At the interface between gold and VO_2, the matching conditions for surface plasmon polariton (SPP) are represented by cyan and magenta lines for the insulating and metallic phases of VO_2, respectively. When VO_2 is in the insulating phase, in the wavelength range of 650-700nm, the absorption efficiency is nearly 1 due to the cavity resonance generated within the slit, regardless of the slit's periodicity. On the other hand, in the metallic phase, SPPs are excited between VO_2 and gold in this wavelength range, and the absorption due to cavity resonance is inhibited.

Figure 4.6(a) illustrates the reflection (solid line) and absorption (dotted line) spectra of VO_2 in the insulating (blue curve) and metallic (red curve) phases when period of Au grating p = 250nm. It shows that the highest absorption occurs at a wavelength of 670nm, while the reflectance is lowest at the same wavelength. As VO_2 transitions from the insulating to the metallic phase, the absorption decreases, and the reflectance increases. Figure 4.6(b) presents the spatial distribution of the

magnetic field intensity at a wavelength of 670 nm. It can be observed that in the metallic phase, cavity resonance decreases, leading to an increase in reflection.

Similarly, Figure 4.6(c) displays the reflection (solid line) and absorption (dotted line) spectra of VO_2 in the insulating (blue curve) and metallic (red curve) phases when period of Au grating p = 300 nm. The highest absorption occurs at a wavelength of 680nm, while the reflectance is lowest at the same wavelength. Figure 4.6(d) shows the spatial distribution of the magnetic field intensity at a wavelength of 680 nm. It demonstrates that in the metallic phase, cavity resonance decreases, resulting in increased reflection.

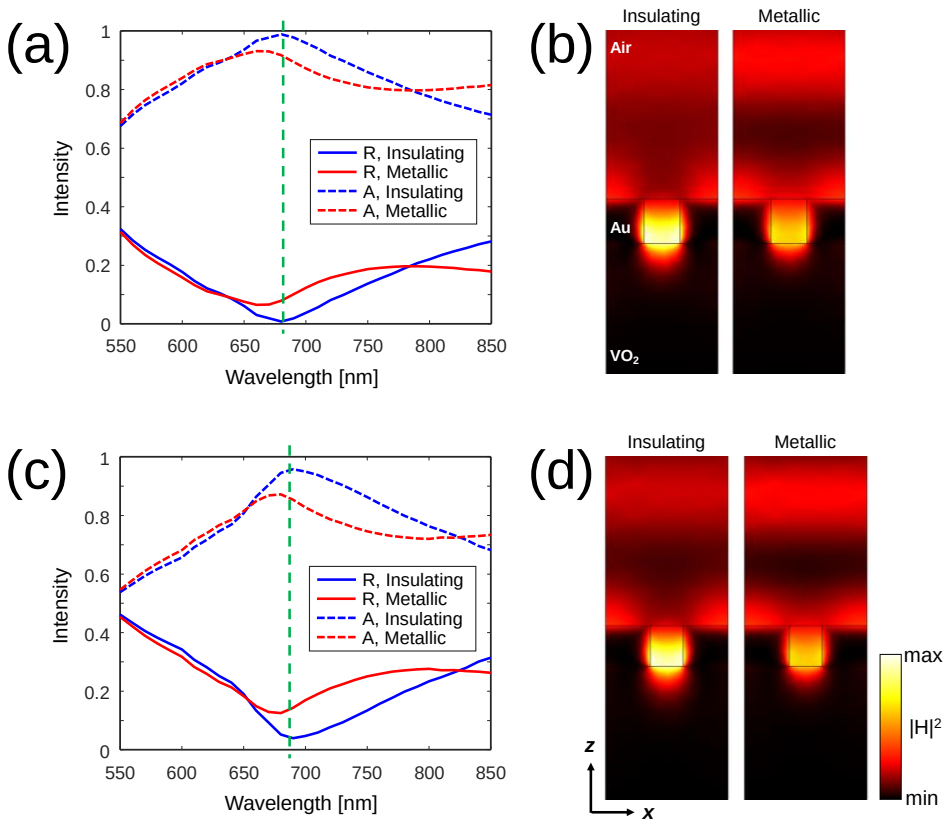

Figure 4.6 (a) Numerically calculated reflectance and absorption spectra of the grating and (b) spatial distribution of magnetic field intensity. Period of grating p = 250 nm and wavelength is 670 nm. (c) Numerically calculated reflectance and absorption spectra of the grating and (d) spatial distribution of magnetic field intensity. Period of grating p = 300 nm and wavelength is 680 nm.

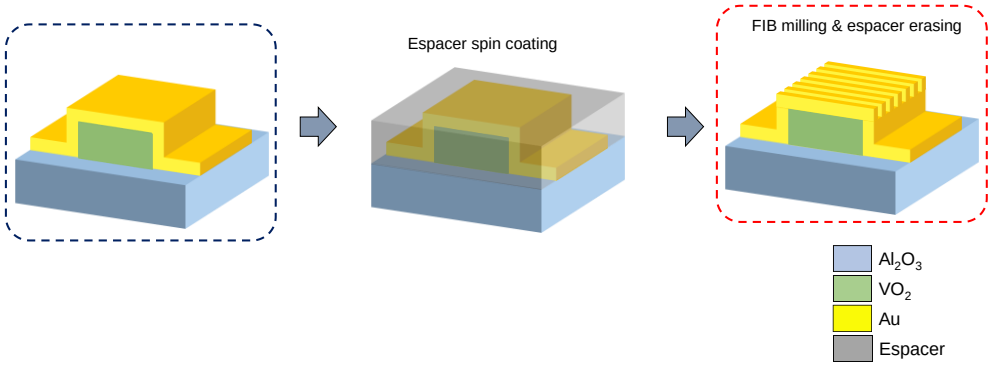

Figure 4.7 Schematic diagram of manufacturing process of VO_2 film with Au nanobeam

Figure 4.7 presents a schematic diagram illustrating the fabrication process of a grating structure. This grating consists of gold nanobeams that are arranged periodically on a VO_2 film, which is accompanied by gold electrical-heating patch. In order to prevent the charging of Ga+ ions during the focused ion beam process, an espacer is applied through spin-coating on the sample, fabricated following the procedure in Figure 4.2. Subsequently, the grating is precisely milled using a FIB instrument (FEI, Quanta 200 3D). Finally, the espacer is erased to complete the sample fabrication. The scanning electron microscope (SEM) images of the fabricated VO_2 extraordinary optical absorption grating are shown in Figure 4.8. These images provide a detailed view of the grating structure and its features. The SEM images reveal the patterned arrangement of the grating with high resolution, allowing for a closer examination of its morphology.

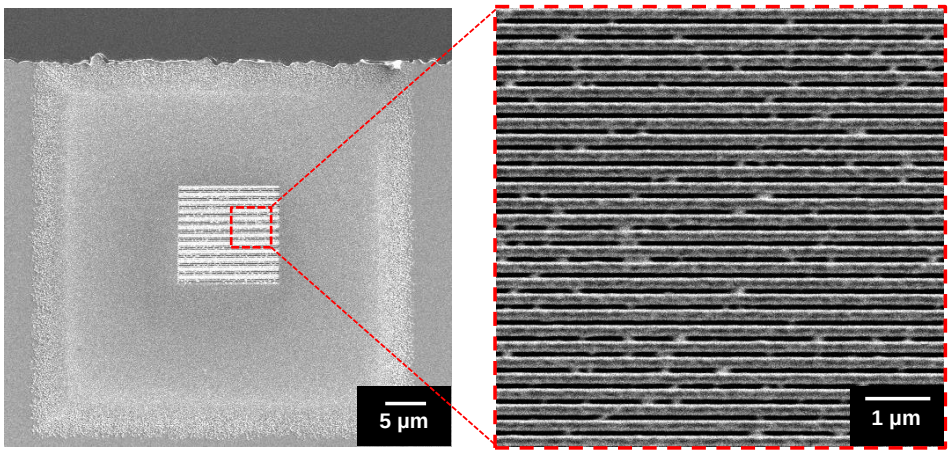

Figure 4.8 Scanning electron microscope images of the fabricated VO_2 extraordinary optical absorption grating

When conducting electro-thermal modulation experiments on VO_2, it is important to exercise caution to prevent device damage. The metal circuitry, being a very thin film, is highly susceptible to oxidation (as shown in Figure 4.9 (a)). Additionally, there is a risk of physical damage when connecting external equipment such as a function generator, as illustrated in Figure 4.9 (b). Furthermore, applying excessive voltage can lead to the failure of the overheated metal circuitry (Figure 4.9(c)) or the burning of the VO_2 layer (Figure 4.9 (d)).

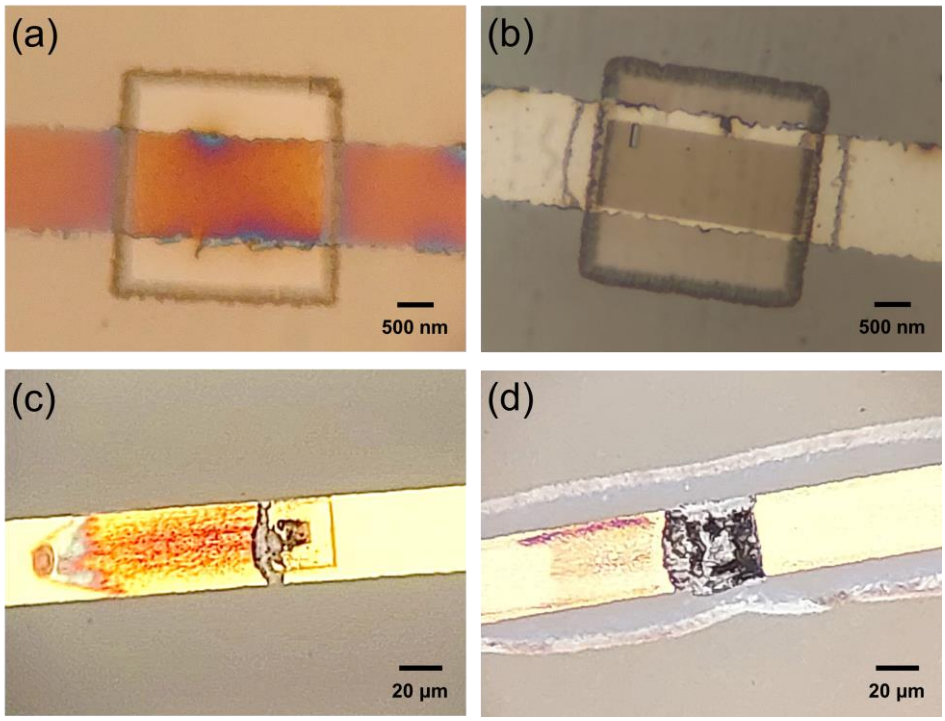

Figure 4.9 Examples of sample damages: (a) oxidation, (b) mechanical damage, (c) melting, (d) burnout

4.5 Conclusion

In this chapter, the experimental studies on high-speed electro-thermal amplitude modulation in the visible-NIR band of VO_2 are presented. When DC power was connected, it was found that the phase of VO_2 changes at 205 mA during an increase in the applied current and at 150 mA during a decrease in the applied current. The experiments also confirmed that the reflectance was modulated whenever the pulse signal was reversed under AC power. A significant observation is that when a pulse voltage of 4.5 V_{pp} with a frequency of 20 Hz was applied, the reflectance modulation was half of that observed when a pulse voltage of 1 Hz with the same magnitude was applied. Additionally, a structure was introduced to enable high-speed electro-thermal reflection amplitude modulation in visible and near-infrared light, and the potential for future development in this area was discussed.

Chapter 5 Conclusion

This dissertation introduces novel research outcomes regarding three metasurface technologies that enable amplitude modulation. These technologies utilize vanadium dioxide thin film, a prominent phase change material, to overcome the limitations of current active metasurface devices.

In chapter 2, developed thermo-optically switchable Fresnel zone plates, based on phase-change metafilms, have been designed and analyzed at a visible wavelength of 660 nm. These metafilms utilize vanadium dioxide (VO_2), a phase-change material with a significant thermo-optic response, to create four distinct plasmonic phase-change absorbers. The zone plates exhibit strong focus switching contrast (40%, 83%) and high numerical apertures (1.52, 1.70), functioning as cylindrical and spherical lenses in reflection. The combination of VO_2's thermo-optic effect and localized plasmonic resonances in the aluminum nanostructures allows for versatile and high-contrast focus-switching performance based on adjustable absorption resonances.

Chapter 3 introduces the proposal and validation of metagrating devices that are optimized based on multiple objectives. This is achieved through the utilization of numerical simulations and experimental studies. These devices achieve an on-state transmittance of approximately 0.3 for unpolarized, independent of wavelength, while exhibiting an average modulation depth of around 0.8. Furthermore, the integration of a metallic thin film micro-heater could enable rapid electrical modulation and pixel-by-pixel phase-change, offering additional functionality.

In chapter4, the experimental studies focus on high-speed electro-thermal amplitude modulation in the visible-NIR band of VO_2. When a direct current (DC) power was applied, it was observed that the phase of VO_2 changed at 205 mA during an increase in the applied current and at 150 mA during a decrease. The experiments also confirmed that the reflectance was modulated whenever the AC pulse signal was reversed under AC power. A significant finding was that when a pulse voltage of 4.5 V_{pp} with a frequency of 20 Hz was applied, the reflectance modulation was approximately half of that observed when a pulse voltage of 1 Hz with the same magnitude was applied.

It is anticipated that this dissertation will make a valuable contribution to the advancement of photo-thermal and electro-thermal active optical devices, facilitating the development of practical technologies in the field of active nano optical devices.

Bibliography

1. N. Yu, P. Genevet, M. A. Kats, F. Aieta, J.-P. Tetienne, F. Capasso, and Z. Gaburro, "Light propagation with phase discontinuities: generalized laws of reflection and refraction," Science 334, 333-337 (2011).
2. D. Lin, P. Fan, E. Hasman, and M. L. Brongersma, "Dielectric gradient metasurface optical elements," Science 345, 298-302 (2014).
3. Y. Kivshar and A. Miroshnichenko, "Meta-optics with Mie resonances," Opt. Photonics News 28, 24-31 (2017).
4. J. P. B. Mueller, N. A. Rubin, R. C. Devlin, B. Groever, and F. Capasso, "Metasurface polarization optics: Independent phase control of arbitrary orthogonal states of polarization," Phys. Rev. Lett. 118, 113901 (2017).
5. A. M. Shaltout, V. M. Shalaev, and M. L. Brongersma, "Spatiotemporal light control with active metasurfaces," Science 364, eaat3100 (2019).
6. F. Aieta, P. Genevet, N. Yu, M. A. Kats, Z. Gaburro, and F. Capasso, "Out-of-plane reflection and refraction of light by anisotropic optical antenna metasurfaces with phase discontinuities," Nano Lett. 12, 1702-1706 (2012).
7. M. Khorasaninejad and F. Capasso, "Broadband multifunctional efficient meta-gratings based on dielectric waveguide phase shifters," Nano Lett. 15, 6709-6715 (2015).
8. Y. Ra'di, D. L. Sounas, and A. Alù, "Metagratings: Beyond the limits of graded metasurfaces for wave front control," Phys. Rev. Lett. 119, 067404 (2017).
9. D. Sell, J. Yang, S. Doshay, R. Yang, and J. A. Fan, "Large-angle, multifunctional metagratings based on freeform multimode geometries," Nano Lett. 17, 3752-3757 (2017).
10. J. Jiang, D. Sell, S. Hoyer, J. Hickey, J. Yang, and J. A. Fan, "Free-form diffractive metagrating design based on generative adversarial networks," ACS Nano 13, 8872-8878 (2019).

11. S.-J. Kim, "Broadband phase-change metagrating design for efficient active reflection steering," Curr. Opt. Photon. 5, 134-140 (2021).
12. M. Khorasaninejad, W. T. Chen, R. C. Devlin, J. Oh, A. Y. Zhu, F. Capasso, "Metalenses at visible wavelengths: Diffraction-limited focusing and subwavelength resolution imaging," Science 352, 1190-1194 (2016).
13. M. Khorasaninejad, A. Y. Zhu, C. Roques-Carmes, W. T. Chen, J. Oh, I. Mishra, R. C. Devlin, and F. Capasso, "Polarization-insensitive metalenses at visible wavelengths," Nano Lett. 16, 7229-7234 (2016).
14. A. Arbabi, E. Arbabi, S. M. Kamali, Y. Horie, S. Han, and A. Faraon, "Miniature optical planar camera based on a wide-angle metasurface doublet corrected for monochromatic aberrations," Nat. Commun. 7, 13682 (2016).
15. A. Arbabi, Y. Horie, M. Bagheri, and A. Faraon, "Dielectric metasurfaces for complete control of phase and polarization with subwavelength spatial resolution and high transmission," Nat. Nanotechnol. 10, 937-943 (2015).
16. S. M. Kamali, E. Arbabi, A. Arbabi, and A. Faraon, "A review of dielectric optical metasurfaces for wavefront control," Nanophotonics 7, 1041-1068 (2018).
17. S.-J. Kim, C. Kim, Y. Kim, J. Jeong, S. Choi, W. Han, J. Kim, and B. Lee, "Dielectric metalens: Properties and three-dimensional imaging applications," Sensors 21, 4584 (2021).
18. C. Kim, S.-J. Kim, and B. Lee, "Doublet metalens design for high numerical aperture and simultaneous correction of chromatic and monochromatic aberrations," Opt. Express 28, 18059-18076 (2020).
19. G.-Y. Lee, J.-Y. Hong, S. Hwang, S. Moon, H. Kang, S. Jeon, H. Kim, J.-H. Jeong, and B. Lee, "Metasurface eyepiece for augmented reality," Nat. Commun. 9, 4562 (2018).
20. Y. Kim, G.-Y. Lee, J. Sung, J. Jang, and B. Lee, "Spiral metalens for phase contrast imaging," Adv. Funct. Mater. 32, 2106050 (2022).
21. Y. Lee, J Yun, M Seo, S.-J. Kim, J. Oh, C. M. Kang, H.-J. Sun, T. D. Chung, and B. Lee, "Full-Color-Tunable Nanophotonic Device Using

Electrochromic Tungsten Trioxide Thin Film," Nano Lett. 20, 8, 6084−6090 (2020).

22. C. Choi, S.-Y. Lee, S.-E. Mun, G.-Y. Lee, J. Sung, H. Yun, J.-H. Yang, H.-O. Kim, C.-Y. Hwang, and B. Lee, "Metasurface with nanostructured $Ge_2Sb_2Te_5$ as a platform for broadband-operating wavefront switch," Advanced Optical Materials 7, 12, 1900171 (2019).
23. C. Choi, S.-E. Mun, J. Sung, K Choi, S.-Y. Lee, and B. Lee, "Hybrid state engineering of phase-change metasurface for all-optical cryptography," Advanced Functional Materials, 31, 4, 2007210 (2021).
24. M. M. Qazilbash, M. Brehm, B.-G. Chae, P.-C. Ho, G. O. Andreev, B.-J. Kim, S. J. Yun, A. V. Balatsky, M. B. Maple, F. Keilmann, H.-T. Kim, and D. N. Basov, "Mott transition in VO_2 revealed by infrared spectroscopy and nano-imaging," Science 318, 1750-1753 (2007).
25. M. J. Dicken, K. Aydin, I. M. Pryce, L. A. Sweatlock, E. M. Boyd, S. Walavalkar, J. Ma, and H. A. Atwater, "Frequency tunable near-infrared metamaterials based on VO_2 phase transition," Opt. Express 17, 18330-18339 (2009).
26. M. M. Qazilbash, A. A. Schafgans, K. S. Burch, S. J. Yun, B. G. Chae, B. J. Kim, H. T. Kim, and D. N. Basov, "Electrodynamics of the vanadium oxides VO_2 and V_2O_3," Phys. Rev. B 77, 115121 (2008).
27. J. Jeong, A. Joushaghani, S. Paradis, D. Alain, and J. K. S. Poon, "Electrically controllable extraordinary optical transmission in gold gratings on vanadium dioxide," Opt. Lett. 40, 4408-4411 (2015).
28. Y. Kim, P. C. Wu, R. Sokhoyan, K. Mauser, R. Glaudell, G. K. Shirmanesh, and H. A. Atwater, "Phase modulation with electrically tunable vanadium dioxide phase-change metasurfaces," Nano Lett. 19, 3961-3968 (2019).
29. S.-J. Kim, H. Yun, K. Park, J. Hong, J.-G. Yun, K. Lee, J. Kim, S. J. Jeong, S.-E. Mun, J. Sung, Y. W. Lee, and B. Lee, "Active directional switching of surface plasmon polaritons using a phase transition material," Sci. Rep. 7, 43723 (2017).

30. S.-J. Kim, S. Choi, C. Choi, Y. Lee, J. Sung, H. Yun, J. Jeong, S.-E. Mun, Y. W. Lee, and B. Lee, "Broadband efficient modulation of light transmission with high contrast using reconfigurable VO_2 diffraction grating," Opt. Express 26, 34641-34654 (2018).
31. S.-J. Kim, I. Kim, S. Choi, H. Yoon, C. Kim, Y. Lee, J. Son, Y. W. Lee, J. Rho, and B. Lee, "Reconfigurable all-dielectric Fano metasurfaces for strong intensity modulations of visible light," Nanoscale Horiz. 5, 1088–1095 (2020).
32. S.-J. Kim, H. Yun, S. Choi, J.-G. Yun, K. Park, S. J. Jeong, S.-Y. Lee, Y. Lee, J. Sung, C. Choi, J. Hong, Y. W. Lee, and B. Lee, "Dynamic phase-change metafilm absorber for strong designer modulation of visible light," Nanophotonics 10, 713-725 (2021).
33. S.-J. Kim, "Diffractive VO_2 metagrating for strong multi-objective amplitude modulation of optical reflection," Appl. Opt. 60, 2483-2487 (2021).
34. J. Park, S. J. Kim, and M. L. Brongersma, "Condition for unity absorption in an ultrathin and highly lossy film in a Gires–Tournois interferometer configuration," Opt. Lett. 40, 1960-1963 (2015).
35. M. A. Kats and F. Capasso, "Optical absorbers based on strong interference in ultra-thin films," Laser Photonics Rev. 10, 735-749 (2016).
36. M. A. Kats, R. Blanchard, P. Genevet, and F. Capasso, "Nanometre optical coatings based on strong interference effects in highly absorbing media," Nat. Mater. 12, 20-24 (2013).
37. M. A. Kats, D. Sharma, J. Lin, P. Genevet, R. Blanchard, Z. Yang, M. M. Qazilbash, D. N. Basov, S. Ramanathan, and F. Capasso, "Ultra-thin perfect absorber employing a tunable phase change material," Appl. Phys. Lett. 101, 221101 (2012).
38. M. Esfandyarpour, E. C. Garnett, Y. Cui, M. D. McGehee, and M. L. Brongersma, "Metamaterial mirrors in optoelectronic devices," Nat. Nanotechnol. 9, 542-547 (2014)

39. A. D. Rakić, "Algorithm for the determination of intrinsic optical constants of metal films: application to aluminum," Appl. Opt. 34, 4755-4767 (1995).
40. I. H. Malitson, "Refraction and Dispersion of Synthetic Sapphire," J. Opt. Soc. Am. 52, 1377-1379 (1962).
41. S. J. Kim, P. Fan, J.-H. Kang, and M. L. Brongersma, "Creating semiconductor metafilms with designer absorption spectra," Nat. Commun. 6, 7591 (2015).
42. S. J. Kim, J. Park, M. Esfandyarpour, E. F. Pecora, P. G. Kik, and M. L. Brongersma, "Superabsorbing, artificial metal films constructed from semiconductor nanoantennas," Nano Lett. 16, 3801-3808 (2016).
43. A. Cordaro, J. van de Groep, S. Raza, E. F. Pecora, F. Priolo, and M. L. Brongersma, "Antireflection high-index metasurfaces combining Mie and Fabry-Pérot resonances," ACS Photonics 6, 453-459 (2019).
44. H. R. Philipp, "Optical properties of silicon nitride," J. Electrochem. Soc. 120, 295-300 (1973).
45. M. M. Elsawy, S. Lanteri, R. Duvigneau, J. A. Fan, and P. Genevet, "Numerical optimization methods for metasurfaces," Laser Photonics Rev. 14, 1900445 (2020).
46. M. Wang, J. S. Lee, S. Aggarwal, N. Farmakidis, Y. He, T. Cheng, and H. Bhaskaran, "Varifocal Metalens Using Tunable and Ultralow-lossDielectrics," Adv. Sci.10, 2204899 (2023).
47. S. Qin, N. Xu, H. Huang, K. Jie, H. Liu, J. Guo, H. Meng, F. Wang, X. Yang, and Z. Wei, "Near-infrared thermally modulated varifocal metalens based on the phase change material Sb_2S_3," Optics Express 29, 5, 7925-7934 (2021).
48. A. Afridi, J. Canet-Ferrer, L. Philippet, J. Osmond, P. Berto, and R. Quidant, "Electrically Driven Varifocal Silicon Metalens," ACS Photonics 5, 4497−4503 (2018).

49. M. Bosch, M. R. Shcherbakov, K. Won, H.-S. Lee, Y. Kim, and G. Shvets "Electrically Actuated Varifocal Lens Based on Liquid-CrystalEmbedded Dielectric Metasurfaces," Nano Lett. 21, 3849−3856 (2021).
50. X. Yin, T. Steinle, L. Huang, T. Taubner, M. Wuttig, T. Zentgraf and H. Giessen, "Beam switching and bifocal zoom lensing using active plasmonic metasurfaces," Light: Science & Applications 6, e17016 (2017).
51. S. Kruk and Y. Kivshar, "Functional meta-optics and nanophotonics governed by Mi e resonances," ACS Photonics 4, 11, 2638-2649 (2017).
52. G.-Y. Lee, J. Sung, and B. Lee. "Metasurface optics for imaging applications," MRS Bulletin 45.3, 202-209 (2020).
53. S. Chen, W. Liu, Z. Li, H. Cheng, and J. Tian, "Metasurface-empowered optical multiplexing and multifunction," Advanced Materials 32, 3, 1805912 (2019).
54. C. Jung, G. Kim, M. Jeong, J. Jang, Z. Dong, T. Badloe, J. K. W. Yang, and J. Rho "Metasurface-driven optically variable devices," Chemical Reviews 121, 21, 13013-13050 (2021).
55. G. Zheng, H. Mühlenbernd, M. Kenney, G. Li, T. Zentgraf, and S. Zhang, "Metasurface holograms reaching 80% efficiency," Nat. Nanotechnol. 10, 4, 308-312 (2015).
56. D. Sell, J. Yang, E. W. Wang, T. Phan, S. Doshay, and J. A. Fan, "Ultra-high-efficiency anomalous refraction with dielectric metasurfaces," ACS Photonics 5, 6, 2402-2407 (2018).
57. A. Komar, R. Paniagua-Domínguez, A. Miroshnichenko, Y. F. Yu, Y. S. Kivshar, A. I. Kuznetsov, and D. Neshev, "Dynamic beam switching by liquid crystal tunable dielectric metasurfaces," ACS Photonics 5, 5, 1742-1748 (2018).
58. M. Decker, C. Kremers, A. Minovich, I. Staude, A. E. Miroshnichenko, D. Chigrin, D. N. Neshev, C. Jagadish, and Y. S. Kivshar "Electro-optical switching by liquid-crystal controlled metasurfaces," Optics Express 21, 7, 8879-8885 (2013).

59. S.-Q. Li, X. Xu, R. M. Veetil, V. Valuckas, R. Paniagua-Domínguez, and A. I. Kuznetsov, "Phase-only transmissive spatial light modulator based on tunable dielectric metasurface," Science 364, 6445, 1087-1090 (2019).
60. Y. -W. Huang, H. W. H. Lee, R. Sokhoyan, R. A. Pala, K. Thyagarajan, S. Han, D. P. Tsai, and H. A. Atwater, "Gate-tunable conducting oxide metasurfaces," Nano letters 16, 9, 5319-5325 (2016).
61. Y. Lee, J. Yun, S.-J. Kim, M. Seo, S. In, H.-D. Jeong, S.-Y. Lee, N. Park, T. D. Chung, and B. Lee, "High-speed transmission control in gate-tunable metasurfaces using hybrid plasmonic waveguide mode," Advanced Optical Materials, 8, 22, 2001256 (2020)
62. J. Park, B. G. Jeong, S. I. Kim, D. Lee, J. Kim, C. Shin, C. B. Lee, T. Otsuka, J. Kyoung, S. Kim, K.-Y. Yang, Y. –Y. Park, J. Lee, I. Hwang, J. Jang, S. H. Song, M. L. Brongersma, K. Ha, S.-W. Hwang, H. Choo and B. L. Choi, "All-solid-state spatial light modulator with independent phase and amplitude control for three-dimensional LiDAR applications," Nature nanotechnology, 16, 1, 69-76 (2021).
63. R. Kaissner, J. Li, W. Lu, X. Li, F. Neubrech, J. Wang, and N. Liu, "Electrochemically controlled metasurfaces with high-contrast switching at visible frequencies," Science Advances 7, 19 (2021).
64. Y. Lee, J. Karst, M. Ubl, M. Hentschel, and H. Giessen, "Dynamic beam control based on electrically switchable nanogratings from conducting polymers," Nanophotonics 12, 14, 2865-2871 (2023).
65. Y. Li, J. van de Groep, A. A. Talin, and M. L. Brongersma, "Dynamic tuning of gap plasmon resonances using a solid-state electrochromic device," Nano Letters, 19, 11, 7988-7995 (2019).
66. E. Arbabi, A. Arbabi, S. M. Kamali, Y. Horie, M. Faraji-Dana, and A. Faraon, "MEMS-tunable dielectric metasurface lens," Nat. Commun. 9, 1, 812 (2018).
67. A. L. Holsteen, S. Raza, P. Fan, P. G. Kik, and M. L. Brongersma, "Purcell effect for active tuning of light scattering from semiconductor optical antennas," Science 358, 6369, 1407-1410 (2017).

68. H. Kwon, T. Zheng, and A. Faraon, "Nano-electromechanical spatial light modulator enabled by asymmetric resonant dielectric metasurfaces," Nat. Commun. 13, 1, 5811 (2022).
69. Q. Wang, E. T. Rogers, B. Gholipour, C. M. Wang, G. Yuan, J. Teng, and N. I. Zheludev "Optically reconfigurable metasurfaces and photonic devices based on phase change materials," Nature Photonics 10, 1, 60-65 (2016).
70. Y. Wang, P. Landreman, D. Schoen, K. Okabe, A. Marshall, U. Celano, H.-S. P. Wong, J. Park, and M. L. Brongersma, "Electrical tuning of phase-change antennas and metasurfaces," Nature Nanotechnology, 16, 6, 667-672 (2021).
71. C. Choi, S.-E. Mun, J. Sung, K Choi, S.-Y. Lee, and B. Lee, "Hybrid state engineering of phase-change metasurface for all-optical cryptography," Advanced Functional Materials 31, 4, 2007210, (2021)
72. N. A. Butakov, I. Valmianski, T. Lewi, C. Urban, Z. Ren, A. A. Mikhailovsky, S. D. Wilson, I. K. Schuller, and J. A. Schuller, "Switchable plasmonic–dielectric resonators with metal–insulator transitions," ACS Photonics, 5, 2, 371-377 (2018).
73. I. Kim, G. Yoon, J. Jang, P. Genevet, K. T. Nam, and J. Rho "Outfitting next generation displays with optical metasurfaces," ACS photonics, 5, 10, 3876-3895 (2018).
74. I. Kim, R. J. Martins, J. Jang, T. Badloe, S. Khadir, H.-Y. Jung, H. Kim, J. Kim, P. Genevet, and J. Rho, "Nanophotonics for light detection and ranging technology," Nature nanotechnology, 16, 5, 508-524 (2021).
75. J. Zhou, Y. Gao, Z. Zhang, H. Luo, C. Cao, Z. Chen, L. Dai and X. Liu, "VO_2 thermochromic smart window for energy savings and generation," Scientific reports 3, 1, 3029 (2013).
76. N. Yu, and F. Capasso, "Optical metasurfaces and prospect of their applications including fiber optics," Journal of Lightwave Technology 33, 12, 2344-2358 (2015).

77. P. Markov, R. E. Marvel, H. J. Conley, K. J. Miller, R. F. Haglund Jr, and S. M. Weiss, "Optically monitored electrical switching in VO_2," Acs Photonics 2, 8, 1175-1182 (2015).
78. C. Kim, and B. Lee, "TORCWA: GPU-accelerated Fourier modal method and gradient-based optimization for metasurface design," Computer Physics Communications 282, 1, 108552 (2023).
79. W. L. Barnes, A. Dereux, and T. W. Ebbesen, "Surface palsmon subwavelength optics, " Nature 424, 6950, 824-830 (2003).
80. T. W. Ebbesen, H. J. Lezec, H. F. Ghaemi, T. Thio, and P. A. Wolff, "Extraordinary optical transmission through sub-wavelength hole arrays, " Nature 391, 6668, 667-669 (1998).

Appendix

Portions of the work discussed in this dissertation were also presented in the following publications:

[Chapter 2]

K. Kim, C. Kim, S.-J. Kim, B. Lee., "Design of Dynamically Focus-switchable Fresnel Zone Plates Based on Plasmonic Phase-change VO_2 Metafilm Absorbers," Current Optics and Photonics, 7, 3, 254-262 (2023).

초 록

메타표면 기술의 등장으로 기존의 수동형 광소자들, 렌즈 프리즘, 편광자, 파장판, 컬러 필터, 거울과 같은 소자들의 극단적인 소형화와 집적화가 가능해지고 있습니다. 한편, 이러한 수동형 메타표면 소자들에서 한걸음 더 나아가서 능동적으로 외부의 변조 시그널 인가에 의해 광학적인 기능을 바꿀 수 있는 능동형 메타표면 소자들이 궁극적인 초박형 광소자 기술로 매우 널리 연구되어 왔습니다. 능동형 메타표면 소자를 구현하기 위한 전략은 간단히 말하여, 외부에서 인가된 전기, 열, 광 에너지에 의해서 굴절률이 변화될 수 있는 능동 광물질들에 나노안테나 공진기 배열로 이루어진 광학 메타표면을 결합시키는 것입니다. 능동형 메타표면은 큰 가능성을 보였지만, 다양한 광학 소자에 메타표면을 적용하기 위해서는 효율, 가시광 변조, 다목적 성능 극대화 등 아직 해결해야 할 과제가 남아 있으며 개선이 필요합니다.

본 학위 논문에서는 기존 능동형 메타표면 소자들의 한계를 극복하기 위하여 대표적인 상변이 물질인 바나듐이산화물 박막을 활용한 3 가지 진폭 변조형 메타표면 기술에 대한 새로운 연구결과를 제시합니다.

먼저 상변화 알루미늄-바나듐이산화물 나노 흡수체를 기반으로 능동 초점 전환이 가능한 FZP 의 새로운 설계 방법과 설계 사례를 제안합니다. 바나듐이산화물의 열광학 효과와 알루미늄 나노구조의 국소화된 플라즈몬 공명 사이의 결합은 크게 조정 가능한 흡수 공명을 기반으로 설계 및 고대비 초점 전환 성능에서 큰 자유도를 제공합니다.

두번째로, 다목적 최적화된 능동메타표면을 제안하였습니다. 제안된 바나듐이산화물 능동메타표면은 편광독립적으로 광대역에서 동작하는 투과율 변조기로써, 고효율을 목표로 하는 두 가지 서로 다른 유형의 회절 메타그레이팅을 설계하고, 이론적 분석과 함께 실험적으로 검증했습니다.

세번째로 가시광-근적외선 영역에서 동작하는 고속 전기-열 진폭변조에 대한 실험적인 연구와 그 결과를 제시합니다. 바나듐이산화물에 금(Au)전열패드를 연결하여 전기적으로 민감하게 반응도록 하였고, 깊은 변조깊이를 가지도록 설계하였습니다.

본 학위 논문에서 제안된 제안된 방법은 비선형 광학, 현미경, 3D 스캐닝, 광학 트래핑 및 가시광선과 적외선 영역을 포함한 넓은 스펙트럼 범위에 걸친 홀로그램 디스플레이를 위한 광열 및 전열 능동 광학 장치에서 큰 잠재력을 가질 수 있습니다.

주요어 : 나노광학, 메타표면, 상변이물질, 바나듐이산화물, 능동 광조절

학 번 : 2013-30959